

# The SAURON project-XXI. The spatially-resolved UV–line strength relations of early-type galaxies

Hyunjin Jeong,<sup>1\*</sup> Sukyoung K. Yi,<sup>2,3</sup> Martin Bureau,<sup>4</sup> Roger L. Davies,<sup>4</sup>  
 Roland Bacon,<sup>5</sup> Michele Cappellari,<sup>4</sup> P. Tim de Zeeuw,<sup>6,7</sup> Eric Emsellem,<sup>5,6</sup>  
 Jesús Falcón-Barroso,<sup>8,9</sup> Davor Krajnović,<sup>6</sup> Harald Kuntschner,<sup>6</sup>  
 Richard M. McDermid,<sup>10</sup> Reynier F. Peletier,<sup>11</sup> Marc Sarzi,<sup>12</sup>  
 Remco C. E. van den Bosch<sup>13</sup> and Glenn van de Ven<sup>13</sup>

<sup>1</sup>*Korea Astronomy and Space Science Institute, Daejeon 305-348, Korea*

<sup>2</sup>*Department of Astronomy, Yonsei University, Seoul 120-749, Korea*

<sup>3</sup>*Yonsei University Observatory, Seoul 120-749, Korea*

<sup>4</sup>*Sub-Department of Astrophysics, University of Oxford, Denys Wilkinson Building, Keble Road, Oxford OX1 3RH*

<sup>5</sup>*Université de Lyon 1, CRAL, Observatoire de Lyon, 9 av. Charles André, F-69230 Saint-Genis Laval; CNRS, UMR 5574, ENS de Lyon, France*

<sup>6</sup>*European Southern Observatory, Karl-Schwarzschild-Str. 2, 85748, Garching, Germany*

<sup>7</sup>*Leiden Observatory, Leiden University, Niels Bohrweg 2, 2333 CA Leiden, the Netherlands*

<sup>8</sup>*Instituto de Astrofísica de Canarias, Vía Láctea s/n, La Laguna, Tenerife, Spain*

<sup>9</sup>*Departamento de Astrofísica, Universidad de La Laguna (ULL), E-38205 La Laguna, Tenerife, Spain*

<sup>10</sup>*Gemini Observatory, 670 North A’Ohoku Place, Hilo, Hawaii 96720, U.S.A.*

<sup>11</sup>*Kapteyn Astronomical Institute, University of Groningen, P.O. Box 800, 9700 AV Groningen, the Netherlands*

<sup>12</sup>*Centre for Astrophysics Research, University of Hertfordshire, Hatfield AL10 9AB*

<sup>13</sup>*Max Planck Institute for Astronomy, D-69117 Heidelberg, Germany*

7 March 2018

## ABSTRACT

The unexpected rising flux of early-type galaxies at decreasing ultraviolet (UV) wavelengths is a long-standing mystery. One important observational constraint is the correlation between UV–optical colours and Mg<sub>2</sub> line strengths found by Burstein et al. (1988). The simplest interpretation of this phenomenon is that the UV strength is related to the Mg line strength. Under this assumption, we expect galaxies with larger Mg gradients to have larger UV colour gradients. By combining UV imaging from *GALEX*, optical imaging from MDM and *SAURON* integral-field spectroscopy, we investigate the spatially-resolved relationships between UV colours and stellar population properties of 34 early-type galaxies from the *SAURON* survey sample. We find that galaxies with old stellar populations show tight correlations between the FUV colours (FUV–V and FUV–NUV) and the Mg *b* index, H $\beta$  index and metallicity [Z/H]. The equivalent correlations for the Fe5015 index,  $\alpha$ -enhancement [ $\alpha$ /Fe] and age are present but weaker. We have also derived logarithmic internal radial colour, *measured* line strength and *derived* stellar population gradients for each galaxy and again found a strong dependence of the FUV–V and FUV–NUV colour gradients on both the Mg *b* line strength and the metallicity gradients for galaxies with old stellar populations. In particular, global gradients of Mg *b* and [Z/H] with respect to the UV colour (e.g.  $\Delta(\text{Mg } b)/\Delta(\text{FUV} - \text{NUV})$  and  $\Delta[\text{Z}/\text{H}]/\Delta(\text{FUV} - \text{NUV})$ ) across galaxies are consistent with their local gradients within galaxies, suggesting that the global correlations also hold locally. From a simple model based on multi-band colour fits of UV upturn and UV-weak galaxies, we have identified a plausible range of parameters that reproduces the observed radial colour profiles. In these models, the centers of elliptical galaxies, where the UV flux is strong, are enhanced in metals by roughly 60% compared to UV-weak regions.

**Key words:** galaxies: elliptical and lenticular, cD – galaxies: evolution – galaxies: photometry – galaxies: stellar content – galaxies: structure – ultraviolet: galaxies

## 1 INTRODUCTION

Far ultraviolet (FUV) radiation was first detected in early-type galaxies (NGC 1291, 1316, 1553, 4406, 4486, 4649 and the bulge of M31) by the *Orbiting Astronomical Observatory-2* in 1969 (Code 1969; Code, Welch & Page 1972). This discovery was surprising, since it had been expected that such old populations would be entirely dark in the FUV. Even more surprisingly, a few elliptical galaxies showed extended *rising* flux for decreasing wavelengths below  $\approx 2000 \text{ \AA}$  (e.g. Code & Welch 1979; Bertola et al. 1980). This was called the UV upturn phenomenon.

Early-on, one of the favored mechanisms for the UV upturn was low-level star formation. Indeed, recent UV imaging surveys from the *Galaxy Evolution Explorer* (*GALEX*) have shown that a very large fraction (at least 15 %) of early-type galaxies as classified by the Sloan Digital Sky Survey (SDSS) exhibit signatures of ongoing or recent star formation (Yi et al. 2005; Schawinski et al. 2007; Kaviraj et al. 2007). In Ultraviolet Imaging Telescope (UIT) images of the centre of M31, however, Bohlin et al. (1985) had not detected point sources suggesting that there is no evidence for the presence of main-sequence O stars even though its UV colour is blue. Furthermore, Welch (1982) claimed that the absence of strong CIV and SiIV in the FUV spectra of M31 indicates that young stellar populations are not present in the bulge of this galaxy.

What, then, is the origin of the UV upturn phenomenon? Early stellar population models reproducing the red colours and spectral energy distributions (SEDs) of early-type galaxies in the optical band suggested that most stars in elliptical galaxies should be old and metal-rich (e.g., Faber 1972; Tinsley 1972), but these models failed to reproduce the strong observed UV flux. It is now generally recognized that early-type galaxies also contain old stellar components with temperatures exceeding 20,000 K. The leading hypothesis suggests that the FUV flux originates from a minority population in the helium-burning horizontal-branch (HB) phase and its progeny, but there are two competing HB solutions: metal-poor (Lee, Demarque & Zinn 1994; Park & Lee 1997; Buzzoni & González-Lópezlira 2008) and metal-rich (Greggio & Renzini 1990; Horch, Demarque & Pinsonneault 1992; Bressan, Chiosi & Fagotto 1994; Dorman, O’Connell & Rood 1995; Yi, Demarque & Kim 1997). It is widely known that metal-poor HB stars can be hot and become UV bright when they are old. The oldest stars in this scenario are the most metal-poor and are most likely to be found in galactic centres, where the UV flux is strong, but the required age is older than that of typical Milky Way globular clusters (Yi et al. 1999). On the other hand, metal-rich HB stars (Bressan et al. 1994; Yi, Demarque & Kim 1997) generate UV sources by skipping the asymptotic giant branch (AGB) phase and require a similar age as the Milky Way halo. This phenomenon, dubbed the AGB manqué stage (Greggio & Renzini 1990), is more pronounced at high values of helium abundance (Horch et al. 1992; Dorman et al. 1995). Metal-rich stars thus become UV-bright sources. A thorough review of these issues is available in O’Connell (1999).

Based on recent observations, a number of studies have

identified peculiar globular clusters with extended horizontal branch (EHB) stars attributable to the presence of super-helium-rich populations (see e.g. Lee et al. 2005; Lee, Gim & Casetti-Dinescu 2007). These studies also discussed the discovery of numerous UV-bright globular clusters in the giant elliptical galaxy M87 (see e.g. Sohn et al. 2006). Although the origin of this helium enhancement is not yet fully understood, it could be a source of the FUV flux in elliptical galaxies. Binary stars offer another possibility: Han et al. (2003), who constructed population synthesis models including binaries, concluded that most UV sources in elliptical galaxies come from binary stars and that there is no temporal evolution in FUV–*V* colour (see e.g. Maxted et al. 2001; Han, Podsiadlowski & Lynas-Gray 2007). The other important candidate is post-AGB (PAGB) stars (e.g. Greggio & Renzini 1990; Dorman et al. 1995; Brown et al. 1997, 2000), which also generate FUV radiation, but are thought to account for only 10 to 30 % of the UV flux.

A crucial observational result is the dependence of the UV upturn on the stellar population and dynamical properties of early-type galaxies (Faber 1983; Burstein et al. 1988, hereafter BBBFL88). BBBFL88 found correlations of the UV–optical colours with both the  $\text{Mg}_2$  index and the central velocity dispersion, based on 24 quiescent early-type galaxies. However, a correlation opposite to the Burstein relation has also been reported. Rich et al. (2005) constructed a FUV–*r* colour from *GALEX* UV and SDSS optical imaging and reported no correlation between the FUV–*r* colour and the  $\text{Mg}_2$  index, even after attempting to exclude galaxies with an active galactic nucleus (AGN) and star formation.

Almost all previous studies focused on integrated UV–line strength relations. However, it is important to look at these relations as a function of radius within galaxies, since this can provide a finer discrimination between UV upturn theories. It has been known that a feature of the UV upturn is the strongest in the centers of early-type galaxies. This produces the positive UV colour gradient that can be interpreted in terms of the difference in the stellar populations (see e.g. O’Connell et al. 1992; O’Connell 1999). Brown et al. (1997) claimed that the FUV light originates in a population with high metallicity and enhanced helium. If the UV colour variation is indeed related to the metal abundance, galaxies with larger metallicity gradients should have larger UV colour gradients. Ohl et al. (1998) found no correlation between the FUV–*B* colour gradients and internal metallicity gradients via the  $\text{Mg}_2$  index, but they had only a small sample.

To reconcile some of these discrepancies, we obtained spatially-resolved galaxy data that can provide detailed information on the stellar population distribution. By combining UV imaging observations from *GALEX* with *SAURON* integral-field early-type galaxy spectroscopy, we re-investigate the relationships originally suggested by BBBFL88. In a companion paper, Bureau et al. (2011, hereafter Paper XVIII) used *GALEX* and *SAURON* data to revisit the integrated UV–line strength relations using identical apertures for all quantities. They recovered correlations of the integrated FUV–*V* and FUV–NUV colours with the integrated  $\text{Mg } b$  line strength index. Furthermore, they argued that most outliers are due to galaxies exhibiting low-level star formation.

In this paper, we focus on the internal gradients of colour, *measured* line strength and *derived* stellar population property within each galaxy. In Section 2, we present a brief summary of the photometric and spectroscopic data and related analyses. The UV-index relations are presented and discussed in Sections 3 and 4. In Section 5, we discuss the origin of the UV upturn phenomenon based on several population synthetic models. We summarize our results and discuss their implications in Section 6.

## 2 OBSERVATIONS AND DATA REDUCTION

### 2.1 UV observations

We observed 34 early-type galaxies from the SAURON sample of 48 (de Zeeuw et al. 2002) with the medium-depth imaging mode of *GALEX* in both FUV (1350–1750 Å) and NUV (1750–2750 Å), as part of our own UV imaging survey of the SAURON sample (*GALEX* guest investigator programmes G11–109 and G13–041) and the *GALEX* Nearby Galaxy Survey (NGS; Gil de Paz et al. 2007). The typical exposure time per field was one orbit ( $\approx 1700$  s), sufficient to exploit the two-dimensional nature of the images. Of the 48 early-type galaxies in the SAURON sample, another 7 galaxies have only short exposures (typically 100–150 s) in the *GALEX* All-sky Imaging Survey (AIS), too shallow for spatially-resolved work. The remaining 7 galaxies have not been observed with *GALEX*, explaining the current sample of 34 as listed in Table 2. Details of the data reduction and analysis for these 34 early-type galaxies are described more fully Jeong et al. (2009, hereafter Paper XIII), so we only summarise our processing here. Details of the *GALEX* instruments, pipeline and calibration are described in Martin et al. (2005) and Morrissey et al. (2005, 2007).

The spatial resolution of the *GALEX* images is approximately  $4''.5$  and  $6''.0$  FWHM in FUV and NUV, respectively, sampled with  $1''.5 \times 1''.5$  pixels. Although the images were delivered after pre-processing, we performed our own sky subtraction by measuring the sky level in source-free regions of the images. Additionally, we convolved the FUV data to the spatial resolution of the NUV observations before any analysis, to avoid spurious colour gradients in the central regions. We also generated a mask image to minimize contamination by nearby sources using SEXTRACTOR, and carefully examined. The mask images are good in most cases, but for a few cases, we had to mask some sources manually. In the case of NGC 4486, for example, we mask the northwestern quadrant to minimize the effect of the jet, but we do not remove the likely contamination by non-thermal UV emission. Finally, we carried out surface photometry by measuring the surface brightness along elliptical annuli using the ELLIPSE task within the STSDAS ISOPHOTE package in IRAF (Image Reduction and Analysis Facility), after masking out nearby sources. For each image, the centre of the isophotes was fixed to the centre of the light distribution and the position angle (PA), ellipticity ( $\epsilon$ ) and surface brightness ( $\mu$ ) were fitted as a function of the radius. The ellipses were fitted only to the NUV images, which have much better signal-to-noise ratios (S/N) at all radii than the FUV images, and these ellipses were then superimposed on the FUV images to derive meaningful colours. We also de-reddened the colours for Galactic

extinction using values of  $A_{\text{FUV}} = 8.376 \times E(B-V)$  and  $A_{\text{NUV}} = 8.741 \times E(B-V)$  (Wyder et al. 2005) and the reddening maps of Schlegel, Finkbeiner & Davis (1998).

### 2.2 Optical observations

Ground-based optical imaging observations with the *Hubble Space Telescope* (*HST*) filter *F555W* (similar to Johnson *V*) were obtained using the MDM Observatory 1.3-m McGraw-Hill Telescope over several observing runs in 2002–2005, again as part of a larger survey targeting the whole SAURON galaxy sample. Details of the MDM observations are described in Falcón-Barroso et al. (2011, hereafter Paper XIX) and the data were reduced and calibrated in the standard manner. The field-of-view of the MDM images is  $17'.3 \times 17'.3$  with  $0''.508 \times 0''.508$  pixels, allowing for accurate sky subtraction and proper sampling of the seeing. The seeing for the observations was  $\approx 1''.2$ .

The MDM data were also convolved to the resolution of the *GALEX* NUV data for the current analysis. The surface brightness profiles were measured after superimposing the NUV ellipses as for the FUV data. The magnitudes at each isophote were then corrected for Galactic extinction using a value of  $R_V = 3.1$  (Cardelli, Clayton & Mathis 1989) and the reddening maps of Schlegel et al. (1998).

### 2.3 SAURON linestrengths and kinematics

The SAURON observations were designed to determine the two-dimensional stellar kinematics (Emsellem et al. 2004, hereafter Paper III; Emsellem et al. 2007, hereafter Paper IX), stellar line strengths and populations (Kuntschner et al. 2006, hereafter Paper VI; Kuntschner et al. 2010, hereafter Paper XVII) and ionised gas kinematics and properties of 48 nearby early-type galaxies in the field and clusters (de Zeeuw et al. 2002), using the panoramic integral-field spectrograph for the William Herschel Telescope (WHT) based on the SAURON TIGER microlens concept. The observations and data reduction are described in the indicated papers.

To explore the UV-line strength relations as a function of radius within individual galaxies, we also imposed the ellipses from the NUV images on the SAURON maps of *measured* line strengths (Mg *b*, Fe5015 and H $\beta$ ), *derived* (as opposed to measured) stellar population properties ( $\alpha$ -enhancement [ $\alpha/\text{Fe}$ ], metallicity [ $\text{Z}/\text{H}$ ] and age) and stellar velocity dispersion ( $\sigma$ ). Paper XVII transformed the Mg *b*, Fe5015, Fe5270 and H $\beta$  line strengths into stellar population properties using the single stellar population (SSP) models of Schiavon (2007). This process is fully described in Paper XVII. It is important to bear in mind that these parameters are derived from only three spectral lines (sometimes four lines), owing to the narrow bandwidth of the SAURON spectra, and that they are “SSP-equivalent” parameters, relying on the supposition that the stars in each galaxy have formed in a single burst. This is an *ad hoc* assumption; however, it allows comparisons between the SSP-equivalent values of different sample galaxies. We use simple luminosity-weighted line strength, population and velocity dispersion averages for each isophote. The legitimacy of this method is discussed in Paper XVIII.

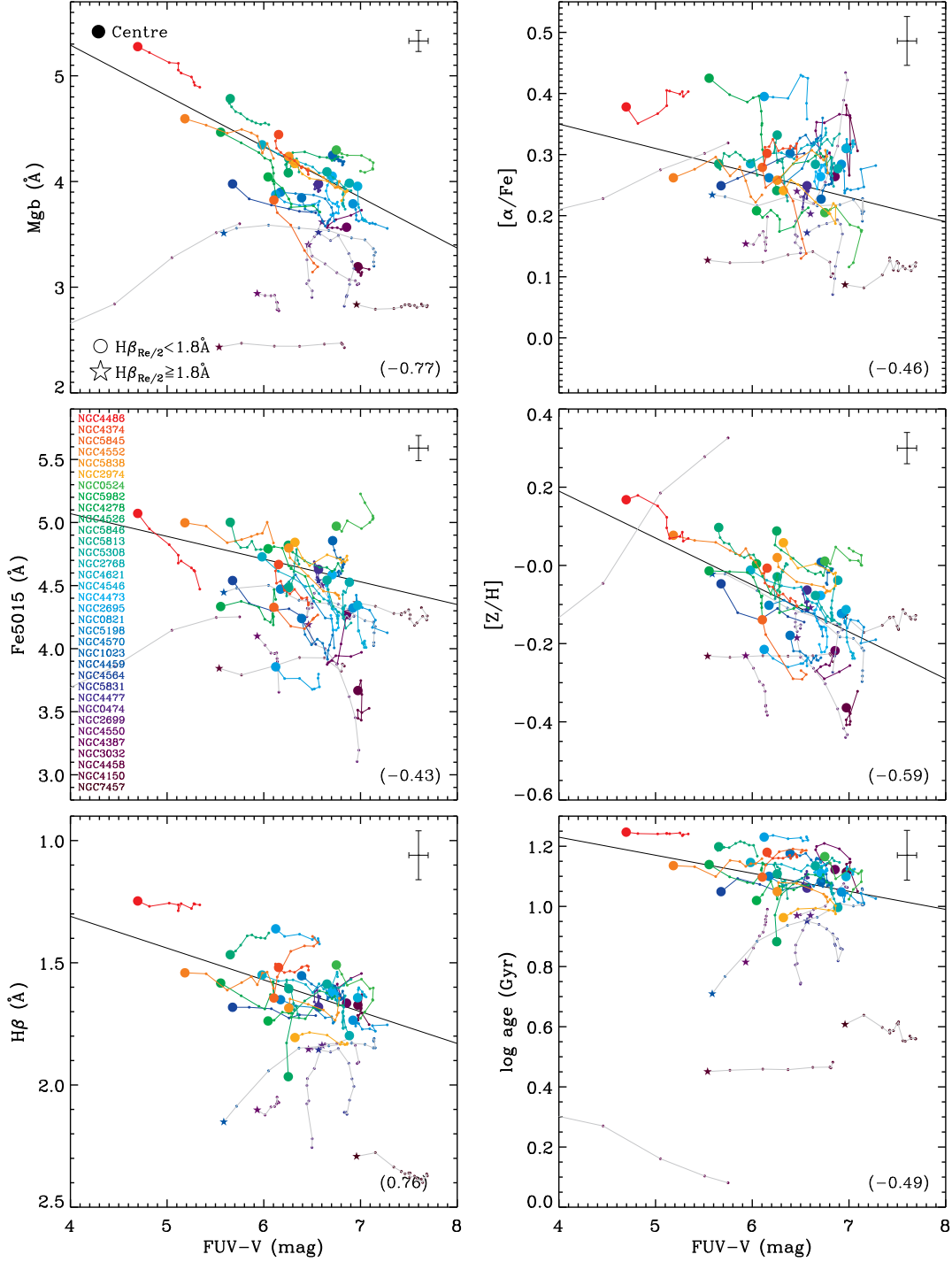


**Figure 1.** UV upturn dependence on *measured* line strengths and *derived* stellar population properties. The Mgb (*top-left*), Fe5015 (*middle-left*), Hβ (*bottom-left*), [α/Fe] (*top-right*), [Z/H] (*middle-right*) and age (*bottom-right*) parameters are shown as a function of the FUV-V colour. We note that all line strengths and *derived* stellar population properties are based on the SAURON data published in Paper VI and Paper XVII, respectively. The sample is divided into quiescent early-type galaxies (circles,  $H\beta_{Re/2} \leq 1.8 \text{ \AA}$ ) and galaxies with recent star formation (stars,  $H\beta_{Re/2} > 1.8 \text{ \AA}$ ). The solid line in each panel is a linear fit to all of the quiescent galaxy profiles, weighting each radius by its V-band luminosity, and the correlation coefficient is reported in the bottom-right corner. The symbols are colour-coded according to the integrated stellar velocity dispersion within one effective radius ( $\sigma_e$ ). All the points for an individual galaxy are represented by a single colour, and the symbol for the central point is larger.



**Table 1.** Parameters of the best-fit linear UV–line strength (and stellar property) relations for old galaxies only.

Colour	Index	Slope	Unit	Zero-point	Unit	Coefficient	Significance level
FUV–V	Mg <i>b</i>	$-0.48 \pm 0.03$	$\text{\AA mag}^{-1}$	$7.97 \pm 0.23$	$\text{\AA}$	-0.77	<0.001
	Fe	$-0.18 \pm 0.04$	$\text{\AA mag}^{-1}$	$6.33 \pm 0.29$	$\text{\AA}$	-0.43	<0.001
	H $\beta$	$0.13 \pm 0.01$	$\text{\AA mag}^{-1}$	$0.58 \pm 0.09$	$\text{\AA}$	0.76	<0.001
	[ $\alpha$ /Fe]	$-0.04 \pm 0.01$	$\text{mag}^{-1}$	$0.55 \pm 0.05$		-0.46	<0.001
	[Z/H]	$-0.12 \pm 0.02$	$\text{mag}^{-1}$	$0.79 \pm 0.08$		-0.59	<0.001
	age	$-0.06 \pm 0.01$	$\text{Gyr mag}^{-1}$	$1.56 \pm 0.05$	Gyr	-0.49	<0.001
	$\sigma_e$	$-0.14 \pm 0.02$	$\text{km s}^{-1} \text{mag}^{-1}$	$3.15 \pm 0.09$	$\text{km s}^{-1}$	-0.54	<0.001
FUV–NUV	Mg <i>b</i>	$-0.73 \pm 0.04$	$\text{\AA mag}^{-1}$	$5.06 \pm 0.05$	$\text{\AA}$	-0.86	<0.001
	Fe	$-0.36 \pm 0.06$	$\text{\AA mag}^{-1}$	$5.09 \pm 0.07$	$\text{\AA}$	-0.59	<0.001
	H $\beta$	$0.19 \pm 0.02$	$\text{\AA mag}^{-1}$	$1.39 \pm 0.03$	$\text{\AA}$	0.72	<0.001
	[ $\alpha$ /Fe]	$-0.03 \pm 0.01$	$\text{mag}^{-1}$	$0.33 \pm 0.01$		-0.29	0.005
	[Z/H]	$-0.20 \pm 0.02$	$\text{mag}^{-1}$	$0.18 \pm 0.02$		-0.72	<0.001
	age	$-0.08 \pm 0.01$	$\text{Gyr mag}^{-1}$	$1.21 \pm 0.01$	Gyr	-0.50	<0.001
	$\sigma_e$	$-0.25 \pm 0.03$	$\text{km s}^{-1} \text{mag}^{-1}$	$2.50 \pm 0.02$	$\text{km s}^{-1}$	-0.68	<0.001

### 3 UV RELATIONS

As argued in the introduction, spatially-resolved galaxy data provide valuable information for discriminating between UV upturn theories. The internal stellar population gradients within each galaxy can yield their own “local” relations, rather than relying on UV–stellar population correlations from the integrated measurements of many galaxies (see e.g. Paper XVIII). When exploring correlations between stellar population parameters and multi-band photometry, our main advantage is that all photometric and spectroscopic measurements are derived using the same ellipses. We note that all stellar absorption line strengths (Mg *b*, Fe5015 and H $\beta$ ), stellar population properties ([ $\alpha$ /Fe], [Z/H] and age) and stellar kinematics ( $\sigma$ ) are based on the SAURON data published in Paper VI, Paper XVII, Paper III and Paper IX.

Strong Balmer absorption lines betray the presence of young stars. Based on the prediction of various stellar population synthesis models (see e.g. Thomas, Maraston & Bender 2003; Schiavon 2007), an H $\beta$  line strength of  $\approx 1.8 \text{\AA}$  can be used to divide the sample into galaxies with effectively only old stellar populations and those which have a contribution from younger stars. To minimise the effects of galaxies with recent star formation on the correlations, we represent galaxies with an integrated H $\beta$  line strength within half an effective radius  $H\beta_{R_{e/2}} > 1.8 \text{\AA}$  (see Table 1 in Paper XVIII) as star symbols (Figures 1–7, 10 and 11). The symbols in Figures 1–7, 10–12 are also colour-coded according to the integrated stellar velocity dispersion within one effective radius ( $\sigma_e$ ; Table A1 in Paper XVII), descending from red to purple.

#### 3.1 Radial profiles

The left-hand panels of Figure 1 show the correlations between the FUV–V colour and the line strength indices Mg *b*, Fe5015 and H $\beta$  as a function of radius. Linear fits to all the quiescent galaxy ( $H\beta_{R_{e/2}} \leq 1.8 \text{\AA}$ ) profiles, after weighting each radius by its luminosity at V band, are shown as solid lines. The value of the correlation coefficient is reported in the bottom-right corner of each panel, and the parameters of the best-fit lines are reported in Table 1, with errors properly taken into account.

The top-left panel of Figure 1 shows the (FUV–V)–Mg *b* “Burstein” relation. This relation shows the tightest correlation among the different line strength indices, as discussed in many previous studies. The slope of a linear fit to the integrated properties of the quiescent galaxies (including the 7 AIS galaxies; see Table 1 of Paper XVIII) is  $-0.40 \pm 0.09 \text{\AA mag}^{-1}$ , whereas the slope measured here based on the luminosity-weighted galaxy profiles (solid line; global gradient) has a value of  $-0.48 \pm 0.03 \text{\AA mag}^{-1}$ . These two slopes are thus consistent within the errors and our results are in good agreement with those of Paper XVIII. All of the quiescent galaxies exhibit bluer FUV–V colours at smaller radii, suggesting that the FUV light is more centrally-concentrated than the optical light, also in agreement with earlier studies (see e.g. Ohl et al. 1998; O’Connell 1999).

We stress that galaxies with young stellar populations ( $H\beta_{R_{e/2}} > 1.8 \text{\AA}$ , star symbols) show different trends (either opposite trends or constant Mg *b* values as FUV–V colours are varied) than quiescent galaxies, so the relation becomes less distinct. These galaxies also have lower Mg *b* values. It is clear therefore that a tight (FUV–V)–Mg *b* relation is only present for galaxies which show no sign of on-going or recent star formation.

The middle-left panel of Figure 1 shows the relation of FUV–V with Fe5015. This relation is much weaker, as found by O’Connell (1999) and Paper XVIII. This implies that the UV strength is more strongly linked to the behavior of the lighter elements (e.g. Mg), not the iron peak.<sup>1</sup> We also note that galaxies with a young population appear at lower Fe values.

In the case of H $\beta$  (bottom-left panel of Figure 1), there is a clear correlation with the FUV–V colour. A tight correlation is, again, only present among quiescent galaxies. The separation of young galaxies (stars) from old ones (circles) is however somewhat artificial in this plot, as we use H $\beta$  itself as the dividing criterion. The observed variation of H $\beta$  with FUV–V is also expected from the (FUV–V)–Mg *b* correlation. According to stellar population models, differences

<sup>1</sup> Admittedly, our analysis is limited to Fe5015 and Mg *b* as iron-peak and magnesium strength indicators due to the narrow wavelength coverage of the SAURON instrument. A wider wavelength coverage is desired to constrain them more robustly.

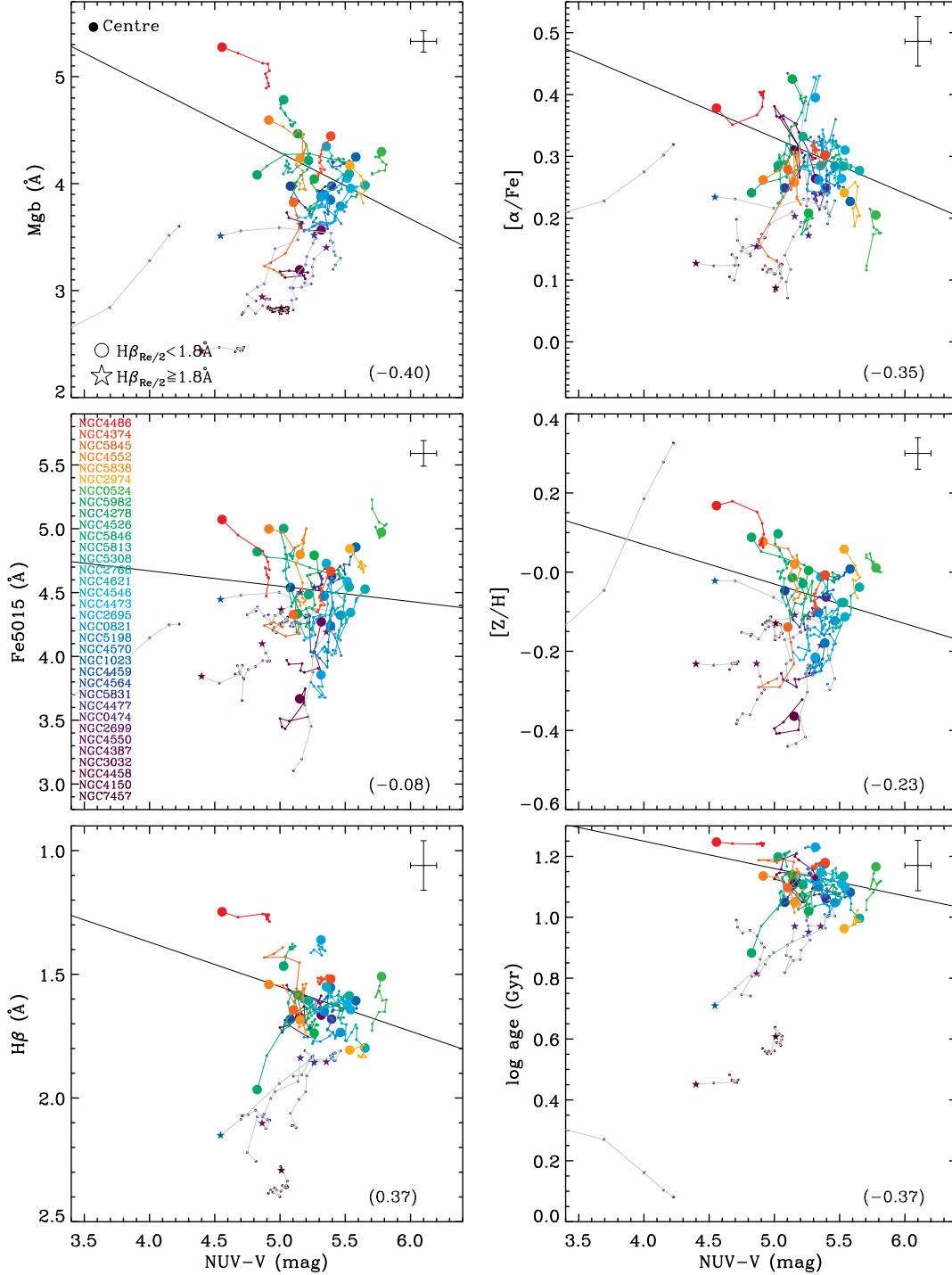


**Figure 2.** Same as Figure 1 but for the  $\text{NUV}-V$  colour.

in metallicity cause variations in the  $\text{H}\beta$  line strength. For example, in the models of Thomas et al. (2003), an  $\text{Mg } b$  value of  $5.16 \text{ \AA}$  and an age of  $12 \text{ Gyr}$  correspond to an  $\text{H}\beta$  line strength of  $1.50 \text{ \AA}$ , whereas for  $\text{Mg } b = 3.11 \text{ \AA}$  and age =  $12 \text{ Gyr}$  the  $\text{H}\beta$  line strength increases to  $1.77 \text{ \AA}$ . The observed trend can thus easily be explained by the effect of metallicity on  $\text{H}\beta$ .

The right-hand panels of Figure 1 show the correlations between the  $\text{FUV}-V$  colour and the stellar population prop-

erties ( $[\alpha/\text{Fe}]$ ,  $[\text{Z}/\text{H}]$  and age) as a function of radius. The parameters of the best-fit lines and the values of the correlation coefficients are again listed in Table 1. Only  $[\text{Z}/\text{H}]$  shows a modest correlation with  $\text{FUV}$ . It is surprising that  $[\alpha/\text{Fe}]$  does not show a clear correlation, considering the tight correlation of  $\text{Mg } b$  with  $\text{FUV}$ .

Analogously to Figure 1, Figure 2 shows the correlations between the  $\text{NUV}-V$  colour and the line strength indices ( $\text{Mg } b$ ,  $\text{Fe}5015$  and  $\text{H}\beta$ ) and stellar population parameters

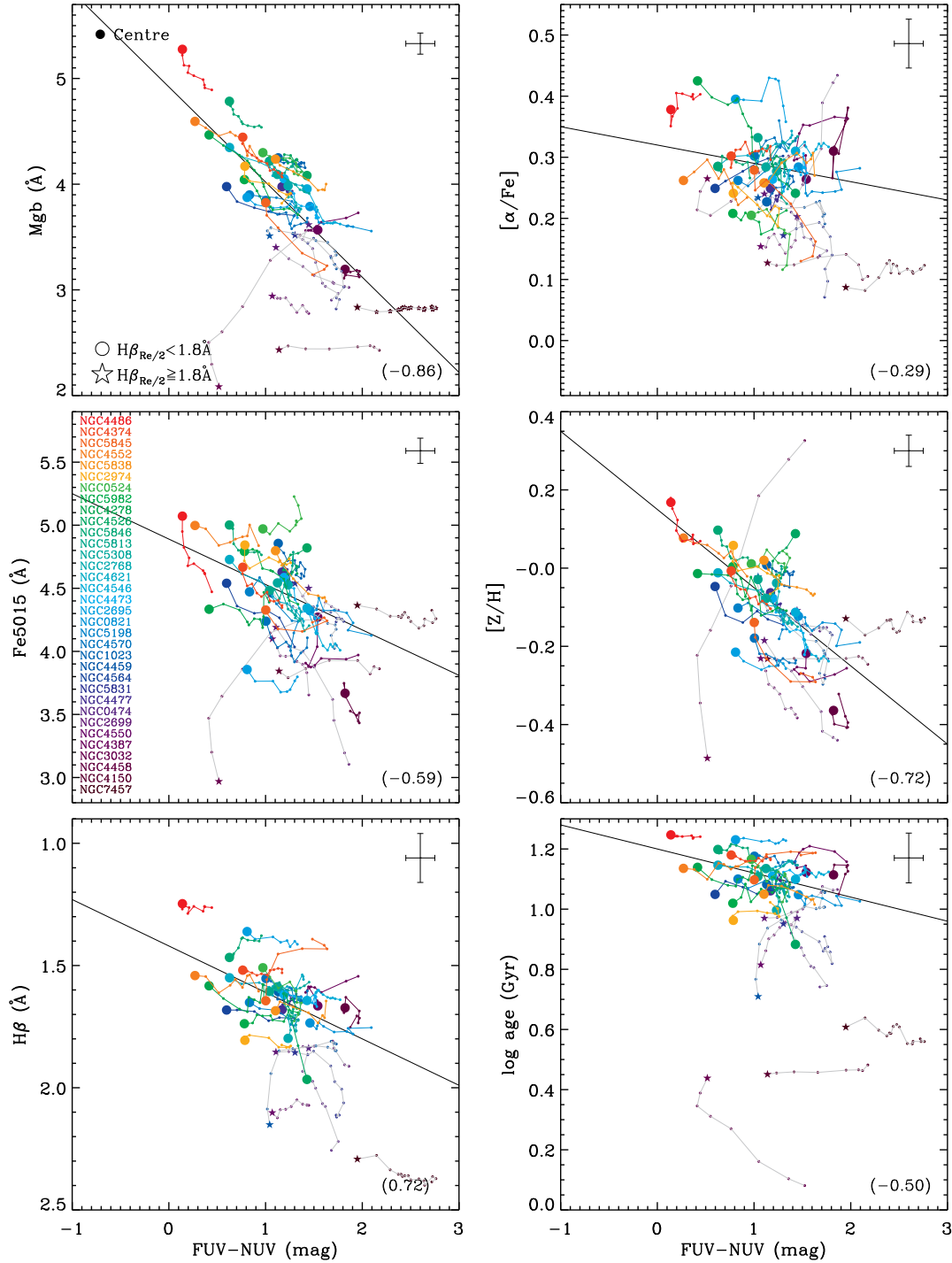


**Figure 3.** Same as Figure 1 but for the FUV–NUV colour.

( $[\alpha/\text{Fe}]$ ,  $[\text{Z}/\text{H}]$  and age) as a function of radius. In contrast to Figure 1, we note no correlation between the NUV–V colour and those quantities. The UV upturn phenomenon clearly dominates the spectral energy distribution only at wavelengths blueward of 2000 Å. We therefore believe that these trends are caused by two main effects: young stars and line blanketing. Recent star formation ( $t \lesssim 1$  Gyr) has a greater effect in the NUV than in the FUV, as only on-going star formation ( $t \lesssim 0.1$  Gyr) can contribute to the

FUV light. On the other hand, line blanketing is significant in the NUV as metallicity increases, as a large number of partially overlapping absorption lines can suppress the continuum. These are probably the main reasons why the FUV correlations become weaker in the NUV. Nevertheless, galaxies with extremely high  $\text{Mg } b$  line strength and a strong UV upturn also show bluer NUV–V colours.

Figure 3 shows the correlations between the FUV–NUV colour and the line strength indices ( $\text{Mg } b$ ,  $\text{Fe5015}$  and  $\text{H}\beta$ )

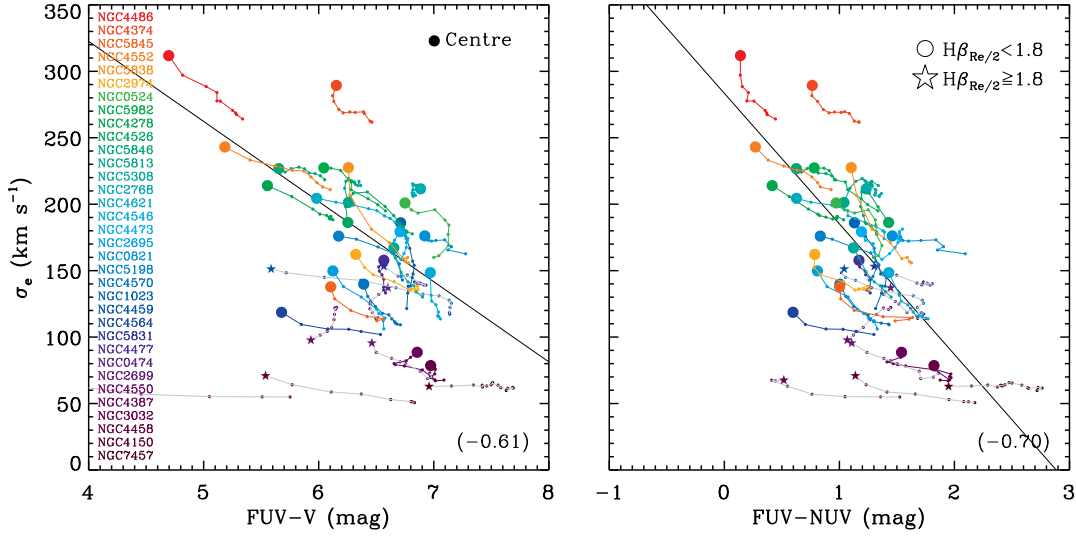


**Figure 4.** Same as Figure 1 but for the FUV–NUV and FUV–V colours as a function of the integrated stellar velocity dispersion within one effective radius  $\sigma_e$ .

and stellar population parameters ( $[\alpha/\text{Fe}]$ ,  $[\text{Z}/\text{H}]$  and age) as a function of radius. The luminosity-weighted linear fits to the data with  $H\beta_{\text{Re}/2} \leq 1.8 \text{ \AA}$  are shown as solid lines and the parameters of the best-fit lines are again reported in Table 1. The value of the correlation coefficient is also reported in the bottom-right corner of each panel and Table 1. Note that the UV–line strength correlations are much more pronounced when the FUV–V colour is replaced by the FUV–NUV colour (see also Donas et al. 2007 and Paper XVIII). For example, the (FUV–NUV)–Mg*b* correlation is tighter than that of (FUV–V)–Mg*b*. We mentioned above that line blanketing is substantial in the NUV and increases with metallicity. This is likely the reason why FUV–NUV correlations are much tighter than those with FUV–V. Another advantage of using FUV–NUV rather than FUV–V is that both FUV and NUV magnitudes are measured with the same instrument, and uncertainties in the UV to optical flux calibration are avoided.

### 3.2 Stellar velocity dispersion

It is well-known that there is a tight correlation between the stellar velocity dispersion ( $\sigma$ ) and the Mg index (see e.g. Terlevich et al. 1981; Bender, Burstein & Faber 1993; Colless et al. 1999; Bernardi et al. 2003). This is a well-studied relation linking a dynamical quantity  $\sigma$  with a quantity (the Mg index) that depends on the stellar populations. A number of studies have implied a correlation of the UV-upturn phenomenon with the stellar velocity dispersion (see e.g. BBBFL88 1988; Donas et al. 2007), a good measure of a galaxy’s gravitational potential depth and total dynamical mass.

Figure 4 shows the colour– $\sigma_e$  relations. Comparing to Figures 1 and 3 (top-left), one can see that the (FUV–V)–Mg*b* and (FUV–NUV)–Mg*b* relations are tighter than the (FUV–V)– $\sigma_e$  and (FUV–NUV)– $\sigma_e$  relations, confirming the results of BBBFL88.

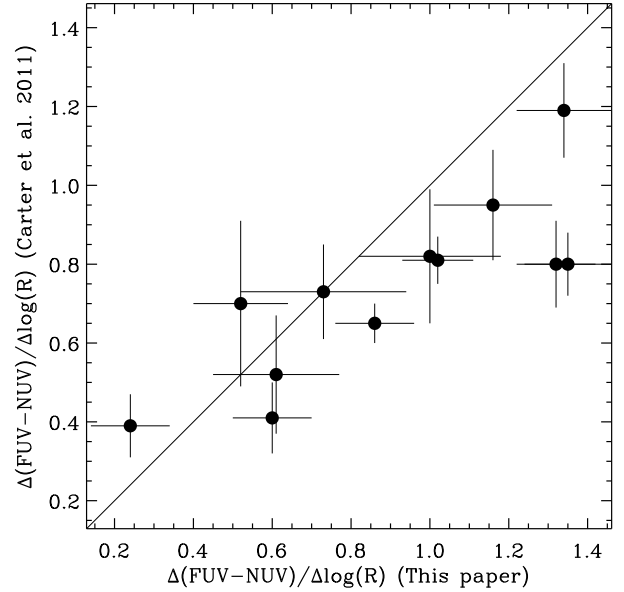


**Figure 5.** Comparison of our (FUV–NUV) radial colour gradients with those of Carter et al. (2011).

### 3.3 Internal gradients

From the radial surface brightness, line strength and stellar population profiles, we derive logarithmic internal radial gradients for each galaxy using least-square fits. The radial range of the fits generally extends from the FWHM of the UV point spread function to half the effective radius ( $R_e/2$ ). The radial gradients are thus defined by their global slopes. In addition, to estimate the gradient uncertainties, we performed Monte-Carlo simulations comprising  $10^3$  realisations, adding noise compatible with the observations to each data point. In Figure 5, we show the comparison of our (FUV–NUV) radial colour gradients with those of Carter et al. (2011). The agreement is generally good: the



**Table 2.** Logarithmic internal radial gradients.

Galaxy	$\frac{\Delta FUV-V}{\Delta \log(R)}$ (mag dex <sup>-1</sup> )	$\frac{\Delta FUV-NUV}{\Delta \log(R)}$ (mag dex <sup>-1</sup> )	$\frac{\Delta Mg b}{\Delta \log(R)}$ (Å dex <sup>-1</sup> )	$\frac{\Delta Fe5015}{\Delta \log(R)}$ (Å dex <sup>-1</sup> )	$\frac{\Delta H\beta}{\Delta \log(R)}$ (Å dex <sup>-1</sup> )	$\frac{\Delta [\alpha/Fe]}{\Delta \log(R)}$	$\frac{\Delta [Z/H]}{\Delta \log(R)}$	$\frac{\Delta \log(\text{age})}{\Delta \log(R)}$ (Gyr dex <sup>-1</sup> )
(1)	(2)	(3)	(4)	(5)	(6)	(7)	(8)	(9)
NGC0474	-0.18 ± 0.16	0.73 ± 0.21	-1.70 ± 0.26	-0.30 ± 0.27	0.89 ± 0.26	-0.17 ± 0.11	-0.14 ± 0.11	-0.52 ± 0.14
NGC0524	0.66 ± 0.14	0.73 ± 0.23	-0.44 ± 0.21	0.44 ± 0.22	0.38 ± 0.21	-0.18 ± 0.08	0.04 ± 0.08	-0.21 ± 0.09
NGC0821	0.44 ± 0.16	1.01 ± 0.26	-0.40 ± 0.21	-0.38 ± 0.21	0.05 ± 0.21	-0.02 ± 0.10	-0.12 ± 0.10	-0.02 ± 0.10
NGC1023	0.14 ± 0.05	0.47 ± 0.10	-0.06 ± 0.16	-0.45 ± 0.16	0.03 ± 0.16	0.08 ± 0.07	-0.07 ± 0.07	0.02 ± 0.08
NGC2695	1.06 ± 0.13	1.24 ± 0.17	-0.26 ± 0.26	-0.19 ± 0.28	0.11 ± 0.26	-0.02 ± 0.10	-0.05 ± 0.10	-0.01 ± 0.05
NGC2699	1.33 ± 0.18	1.81 ± 0.23	-0.89 ± 0.26	-2.50 ± 0.29	0.10 ± 0.26	0.57 ± 0.11	-0.63 ± 0.11	0.28 ± 0.14
NGC2768	-0.06 ± 0.06	0.24 ± 0.10	-0.43 ± 0.17	-0.41 ± 0.17	-0.18 ± 0.17	-0.03 ± 0.08	-0.17 ± 0.08	0.07 ± 0.09
NGC2974	1.31 ± 0.09	1.19 ± 0.16	-0.65 ± 0.23	-0.19 ± 0.23	0.09 ± 0.22	-0.12 ± 0.09	-0.21 ± 0.09	0.08 ± 0.11
NGC3032	7.59 ± 0.11	2.67 ± 0.15	3.62 ± 0.27	3.18 ± 0.29	1.52 ± 0.26	0.22 ± 0.11	2.01 ± 0.12	-0.90 ± 0.08
NGC4150	3.29 ± 0.15	2.74 ± 0.20	0.01 ± 0.26	0.10 ± 0.26	0.11 ± 0.26	-0.05 ± 0.10	-0.01 ± 0.10	0.05 ± 0.09
NGC4278	0.87 ± 0.05	1.02 ± 0.09	-1.01 ± 0.18	-0.01 ± 0.19	-0.02 ± 0.18	-0.23 ± 0.08	-0.26 ± 0.08	0.08 ± 0.08
NGC4374	0.75 ± 0.05	0.86 ± 0.10	-0.64 ± 0.17	-0.53 ± 0.17	0.01 ± 0.17	0.02 ± 0.07	-0.17 ± 0.07	-0.02 ± 0.07
NGC4387	-0.10 ± 0.14	0.43 ± 0.18	0.31 ± 0.23	-0.48 ± 0.24	-0.20 ± 0.22	0.22 ± 0.10	-0.08 ± 0.10	0.14 ± 0.10
NGC4458	0.09 ± 0.16	0.36 ± 0.21	0.04 ± 0.26	-0.53 ± 0.27	0.17 ± 0.26	0.12 ± 0.13	0.06 ± 0.13	-0.07 ± 0.13
NGC4459	2.82 ± 0.13	1.58 ± 0.15	-0.63 ± 0.17	-0.84 ± 0.17	-0.53 ± 0.17	-0.05 ± 0.07	-0.51 ± 0.07	0.56 ± 0.09
NGC4473	0.08 ± 0.12	0.61 ± 0.16	-0.58 ± 0.16	-0.70 ± 0.16	0.01 ± 0.16	0.05 ± 0.07	-0.22 ± 0.07	0.02 ± 0.08
NGC4477	0.10 ± 0.08	0.24 ± 0.13	-0.16 ± 0.26	-0.17 ± 0.26	-0.06 ± 0.26	0.00 ± 0.11	-0.10 ± 0.11	0.10 ± 0.12
NGC4486	1.22 ± 0.13	0.85 ± 0.21	-0.87 ± 0.24	-1.15 ± 0.24	0.02 ± 0.23	0.10 ± 0.09	-0.28 ± 0.09	-0.01 ± 0.02
NGC4526	1.25 ± 0.12	0.07 ± 0.13	0.16 ± 0.21	-0.40 ± 0.21	-0.49 ± 0.21	0.11 ± 0.08	-0.20 ± 0.08	0.34 ± 0.11
NGC4546	0.20 ± 0.07	0.67 ± 0.11	-0.63 ± 0.22	-0.56 ± 0.23	0.03 ± 0.22	0.01 ± 0.11	-0.22 ± 0.11	0.01 ± 0.11
NGC4550	0.42 ± 0.12	0.86 ± 0.16	-0.36 ± 0.23	-0.66 ± 0.24	-0.11 ± 0.23	0.04 ± 0.11	-0.32 ± 0.11	0.34 ± 0.13
NGC4552	1.91 ± 0.04	1.35 ± 0.11	-0.68 ± 0.23	-0.13 ± 0.24	0.04 ± 0.22	-0.11 ± 0.09	-0.18 ± 0.09	0.05 ± 0.08
NGC4564	2.49 ± 0.20	2.05 ± 0.23	-0.75 ± 0.35	-1.10 ± 0.37	0.12 ± 0.34	0.16 ± 0.15	-0.22 ± 0.15	-0.01 ± 0.17
NGC4570	0.64 ± 0.08	0.87 ± 0.10	-0.38 ± 0.21	-0.33 ± 0.22	0.16 ± 0.21	0.04 ± 0.10	-0.09 ± 0.10	-0.06 ± 0.09
NGC4621	1.32 ± 0.06	1.32 ± 0.10	-0.67 ± 0.17	-0.86 ± 0.17	-0.02 ± 0.17	0.09 ± 0.08	-0.23 ± 0.08	0.04 ± 0.07
NGC5198	1.40 ± 0.18	1.22 ± 0.24	-0.68 ± 0.29	-1.28 ± 0.30	0.25 ± 0.29	0.25 ± 0.13	-0.22 ± 0.13	-0.02 ± 0.14
NGC5308	0.67 ± 0.13	0.86 ± 0.17	-0.50 ± 0.29	-0.95 ± 0.30	-0.03 ± 0.29	0.11 ± 0.13	-0.20 ± 0.13	0.06 ± 0.14
NGC5813	0.22 ± 0.06	0.52 ± 0.12	-0.02 ± 0.19	0.54 ± 0.19	0.27 ± 0.19	-0.18 ± 0.08	0.13 ± 0.08	-0.17 ± 0.08
NGC5831	0.58 ± 0.13	1.00 ± 0.18	-1.45 ± 0.21	-0.50 ± 0.22	0.62 ± 0.21	-0.20 ± 0.09	-0.26 ± 0.09	-0.16 ± 0.11
NGC5838	1.29 ± 0.27	1.32 ± 0.38	-0.69 ± 0.26	-0.95 ± 0.27	0.05 ± 0.26	0.07 ± 0.11	-0.20 ± 0.11	-0.11 ± 0.13
NGC5845	1.34 ± 0.33	1.82 ± 0.42	-1.88 ± 0.31	-0.21 ± 0.31	-0.60 ± 0.29	-0.41 ± 0.13	-0.37 ± 0.13	0.14 ± 0.10
NGC5846	0.79 ± 0.04	0.60 ± 0.10	-0.49 ± 0.18	-0.48 ± 0.19	-0.19 ± 0.18	0.00 ± 0.08	-0.17 ± 0.08	0.01 ± 0.06
NGC5982	1.11 ± 0.13	1.16 ± 0.15	-0.72 ± 0.23	-0.90 ± 0.23	-0.08 ± 0.22	-0.02 ± 0.09	-0.25 ± 0.09	0.08 ± 0.11
NGC7457	1.00 ± 0.13	1.09 ± 0.15	0.03 ± 0.14	-0.15 ± 0.14	0.15 ± 0.14	0.04 ± 0.05	0.03 ± 0.05	-0.09 ± 0.06

Columns: (1) Galaxy identifier. (2)–(3): Radial colour gradients. (4)–(9): Radial line strength and stellar population gradients.

mean of the absolute value of the (FUV–NUV) radial colour gradient difference is  $\approx 0.55$  mag dex<sup>-1</sup>. The largest difference is found for NGC 4552 likely due to the determination of the radial range of the fits. We adopted the same radial range to derive the internal radial gradients for each galaxy. The logarithmic internal radial gradients of the UV colours, line strengths and stellar population properties are listed in Table 2.

We plot the internal gradients of the line strength indices and the stellar population parameters as a function of the FUV–V internal colour gradients in Figure 6. To prevent any dilution of the correlation attributable to galaxies with recent star formation, we exclude galaxies with evidence of young stars ( $H\beta_{R_{e/2}} > 1.8$  Å) from the fit and plot them as grey stars. The value of the correlation coefficient is reported in the bottom-right corner of each panel, and the parameters of the best-fit lines are reported in Table 3.

Most importantly, only Mg b and [Z/H] internal gradients for quiescent galaxies show correlations. This suggests that either Mg is a primary driver of the UV upturn, given that Mg b is a reliable tracer of Mg, or Mg and the UV upturn share the same primary driver. If the stellar population

properties ([ $\alpha$ /Fe], [Z/H] and age) are reliable, we conclude further that the UV strength is not predominantly governed by the  $\alpha$ -enhancement. The correlation between the [Z/H] index and the UV colour can be attributed to the role of Mg in the [Z/H] measurement. The weak or absent correlation with  $\alpha$ -enhancement ([ $\alpha$ /Fe]), however, is contrary to our expectations.

Analogously to Figure 6, Figure 7 shows the FUV–NUV logarithmic internal radial colour gradients versus the internal gradients of the line indices and stellar population properties. The (FUV–NUV)–Mg b correlation is again much tighter than the (FUV–V)–Mg b correlation, as discussed in Section 3.1, and the correlation with Mg b is much stronger than that with [Z/H].

Figure 8 shows the internal gradients of the velocity dispersion as a function of the UV internal colour gradients. Comparing to Figures 6 and 7, the correlations with  $\sigma_e$  are much weaker than those with both Mg b and [Z/H]. This suggests that the UV upturn is driven by stellar population properties rather than the velocity dispersion.

For clarity, we divide galaxies into groups exhibiting similar UV radial colour profiles for the region interior to

**Table 3.** Parameters of the best-fit linear radial gradients for old galaxies only.

Colour	Index	Slope	Zero-point	Coefficient	Significance level
FUV–V/ $\Delta\log(R)$	Mg b/ $\Delta\log(R)$	$-0.35 \pm 0.13$	$-0.22 \pm 0.12$	-0.59	0.001
	Fe/ $\Delta\log(R)$	$-0.21 \pm 0.16$	$-0.30 \pm 0.15$	-0.31	0.14
	H $\beta$ / $\Delta\log(R)$	$-0.01 \pm 0.09$	$0.01 \pm 0.07$	-0.07	0.67
	[ $\alpha$ /Fe]/ $\Delta\log(R)$	$-0.01 \pm 0.05$	$0.01 \pm 0.05$	-0.07	0.68
	[Z/H] / $\Delta\log(R)$	$-0.08 \pm 0.04$	$-0.09 \pm 0.04$	0.61	<0.001
	log age/ $\Delta\log(R)$	$0.02 \pm 0.04$	$-0.01 \pm 0.04$	0.21	0.28
FUV–NUV/ $\Delta\log(R)$	log $\sigma_e$ / $\Delta\log(R)$	$-0.30 \pm 0.04$	$-0.12 \pm 0.04$	-0.21	0.27
	Mg b/ $\Delta\log(R)$	$-0.71 \pm 0.16$	$0.10 \pm 0.14$	-0.83	<0.001
	Fe/ $\Delta\log(R)$	$-0.31 \pm 0.25$	$-0.20 \pm 0.23$	-0.31	0.14
	H $\beta$ / $\Delta\log(R)$	$0.13 \pm 0.13$	$-0.10 \pm 0.11$	0.44	0.018
	[ $\alpha$ /Fe]/ $\Delta\log(R)$	$-0.07 \pm 0.08$	$0.05 \pm 0.07$	-0.28	0.18
	[Z/H] / $\Delta\log(R)$	$-0.11 \pm 0.06$	$-0.06 \pm 0.06$	0.54	0.004
	log age/ $\Delta\log(R)$	$-0.03 \pm 0.06$	$0.04 \pm 0.06$	-0.20	0.31
	log $\sigma_e$ / $\Delta\log(R)$	$-0.08 \pm 0.06$	$-0.09 \pm 0.05$	-0.30	0.15

**Table 4.** Internal gradients.

Galaxy	$\frac{\Delta\log\sigma}{\Delta\text{FUV-V}}$ (dex mag <sup>-1</sup> )	$\frac{\Delta\log\sigma}{\Delta\text{FUV-NUV}}$ (dex mag <sup>-1</sup> )	$\frac{\Delta\text{Mgb}}{\Delta\text{FUV-V}}$ (Å mag <sup>-1</sup> )	$\frac{\Delta\text{Mgb}}{\Delta\text{FUV-NUV}}$ (Å mag <sup>-1</sup> )	$\frac{\Delta[\text{Z/H}]}{\Delta\text{FUV-V}}$ (dex mag <sup>-1</sup> )	$\frac{\Delta[\text{Z/H}]}{\Delta\text{FUV-NUV}}$ (dex mag <sup>-1</sup> )	UV type
(1)	(2)	(3)	(4)	(5)	(6)	(7)	(8)
NGC0474	$0.28 \pm 0.15$	$-0.22 \pm 0.07$	$2.59 \pm 0.72$	$-1.94 \pm 0.32$	$0.26 \pm 0.30$	$-0.15 \pm 0.14$	RSF
NGC0524	$-0.14 \pm 0.05$	$-0.19 \pm 0.05$	$-0.40 \pm 0.24$	$-0.47 \pm 0.25$	$-0.02 \pm 0.10$	$0.02 \pm 0.10$	UV-weak
NGC0821	$-0.09 \pm 0.07$	$-0.05 \pm 0.04$	$-0.49 \pm 0.31$	$-0.28 \pm 0.17$	$-0.17 \pm 0.14$	$-0.09 \pm 0.08$	UV-weak
NGC1023	$-0.79 \pm 0.16$	$-0.50 \pm 0.07$	$-0.48 \pm 0.74$	$-0.18 \pm 0.31$	$-0.14 \pm 0.31$	$-0.11 \pm 0.13$	RSF
NGC2695	$-0.28 \pm 0.05$	$-0.26 \pm 0.04$	$-0.20 \pm 0.22$	$-0.20 \pm 0.21$	$-0.04 \pm 0.09$	$-0.04 \pm 0.08$	UVX
NGC2699	$-0.24 \pm 0.04$	$-0.18 \pm 0.03$	$-0.64 \pm 0.18$	$-0.49 \pm 0.14$	$-0.47 \pm 0.08$	$-0.35 \pm 0.06$	UV-weak
NGC2768	$0.04 \pm 0.32$	$-0.13 \pm 0.14$	$2.39 \pm 1.52$	$-1.50 \pm 0.66$	$1.21 \pm 0.66$	$-0.54 \pm 0.29$	UV-weak
NGC2974	$-0.12 \pm 0.04$	$-0.13 \pm 0.04$	$-0.46 \pm 0.17$	$-0.47 \pm 0.18$	$-0.14 \pm 0.07$	$-0.14 \pm 0.07$	RSF
NGC3032	$-0.04 \pm 0.01$	$-0.09 \pm 0.02$	$0.49 \pm 0.04$	$1.24 \pm 0.10$	$0.26 \pm 0.02$	$0.60 \pm 0.04$	RSF
NGC4150	$-0.10 \pm 0.02$	$-0.12 \pm 0.02$	$0.01 \pm 0.08$	$0.01 \pm 0.09$	$0.00 \pm 0.03$	$0.00 \pm 0.04$	RSF
NGC4278	$-0.10 \pm 0.04$	$-0.09 \pm 0.04$	$-0.87 \pm 0.18$	$-0.89 \pm 0.17$	$-0.20 \pm 0.07$	$-0.21 \pm 0.07$	UVX
NGC4374	$-0.08 \pm 0.05$	$-0.08 \pm 0.04$	$-0.83 \pm 0.24$	$-0.75 \pm 0.21$	$-0.22 \pm 0.10$	$-0.20 \pm 0.09$	UVX
NGC4387	$-0.12 \pm 0.07$	$-0.14 \pm 0.04$	$0.40 \pm 0.30$	$0.32 \pm 0.19$	$0.05 \pm 0.12$	$0.00 \pm 0.08$	UV-weak
NGC4458	$-0.26 \pm 0.21$	$-0.27 \pm 0.11$	$-0.04 \pm 0.99$	$0.05 \pm 0.53$	$0.58 \pm 0.44$	$-0.22 \pm 0.27$	UV-weak
NGC4459	$-0.06 \pm 0.01$	$-0.12 \pm 0.02$	$-0.17 \pm 0.05$	$-0.38 \pm 0.10$	$-0.15 \pm 0.02$	$-0.30 \pm 0.04$	RSF
NGC4473	$0.01 \pm 0.15$	$0.03 \pm 0.05$	$-1.33 \pm 0.68$	$-0.84 \pm 0.24$	$-0.54 \pm 0.31$	$-0.32 \pm 0.11$	UV-weak
NGC4477	$-0.75 \pm 0.41$	$-0.55 \pm 0.20$	$-0.53 \pm 1.92$	$-0.58 \pm 0.96$	$-0.44 \pm 0.82$	$-0.36 \pm 0.41$	UV-weak
NGC4486	$-0.11 \pm 0.04$	$-0.18 \pm 0.07$	$-0.60 \pm 0.17$	$-1.08 \pm 0.31$	$-0.19 \pm 0.07$	$-0.33 \pm 0.12$	UVX
NGC4526	$-0.08 \pm 0.03$	$-0.17 \pm 0.10$	$0.08 \pm 0.16$	$-0.53 \pm 0.45$	$-0.15 \pm 0.07$	$0.35 \pm 0.18$	RSF
NGC4546	$-1.03 \pm 0.23$	$-0.33 \pm 0.07$	$-3.03 \pm 1.10$	$-0.93 \pm 0.33$	$-1.03 \pm 0.52$	$-0.33 \pm 0.16$	UV-weak
NGC4550	$0.44 \pm 0.11$	$0.26 \pm 0.06$	$-0.66 \pm 0.48$	$-0.43 \pm 0.27$	$-0.64 \pm 0.22$	$-0.37 \pm 0.13$	RSF
NGC4552	$-0.06 \pm 0.03$	$-0.09 \pm 0.04$	$-0.34 \pm 0.12$	$-0.49 \pm 0.17$	$-0.09 \pm 0.05$	$-0.13 \pm 0.07$	UVX
NGC4564	$-0.07 \pm 0.03$	$-0.08 \pm 0.04$	$-0.30 \pm 0.14$	$-0.35 \pm 0.17$	$-0.09 \pm 0.06$	$-0.10 \pm 0.08$	UVX
NGC4570	$-0.31 \pm 0.07$	$-0.23 \pm 0.05$	$-0.60 \pm 0.31$	$-0.40 \pm 0.24$	$-0.14 \pm 0.15$	$-0.11 \pm 0.12$	UV-weak
NGC4621	$-0.08 \pm 0.03$	$-0.09 \pm 0.03$	$-0.48 \pm 0.12$	$-0.49 \pm 0.13$	$-0.16 \pm 0.06$	$-0.17 \pm 0.06$	UVX
NGC5198	$-0.15 \pm 0.04$	$-0.15 \pm 0.04$	$-0.39 \pm 0.19$	$-0.39 \pm 0.21$	$-0.13 \pm 0.09$	$-0.14 \pm 0.09$	UVX
NGC5308	$-0.41 \pm 0.09$	$-0.33 \pm 0.07$	$-0.76 \pm 0.44$	$-0.60 \pm 0.34$	$-0.31 \pm 0.20$	$-0.24 \pm 0.15$	UV-weak
NGC5813	$0.04 \pm 0.15$	$0.07 \pm 0.08$	$0.10 \pm 0.70$	$-0.10 \pm 0.36$	$0.59 \pm 0.30$	$0.23 \pm 0.15$	A/Z
NGC5831	$-0.12 \pm 0.06$	$-0.08 \pm 0.04$	$-1.33 \pm 0.30$	$-1.20 \pm 0.20$	$-0.20 \pm 0.13$	$-0.19 \pm 0.09$	A/Z
NGC5838	$-0.27 \pm 0.04$	$-0.28 \pm 0.04$	$-0.50 \pm 0.18$	$-0.52 \pm 0.18$	$-0.14 \pm 0.07$	$-0.15 \pm 0.08$	UV-weak
NGC5845	$-0.17 \pm 0.05$	$-0.11 \pm 0.03$	$-1.44 \pm 0.23$	$-0.96 \pm 0.16$	$-0.30 \pm 0.10$	$-0.20 \pm 0.07$	A/Z
NGC5846	$-0.03 \pm 0.05$	$-0.04 \pm 0.06$	$-0.54 \pm 0.22$	$-0.65 \pm 0.28$	$-0.19 \pm 0.09$	$-0.22 \pm 0.11$	UVX
NGC5982	$-0.14 \pm 0.04$	$-0.13 \pm 0.04$	$-0.59 \pm 0.20$	$-0.59 \pm 0.20$	$-0.20 \pm 0.08$	$-0.21 \pm 0.08$	UVX
NGC7457	$-0.02 \pm 0.03$	$-0.02 \pm 0.03$	$0.02 \pm 0.14$	$0.02 \pm 0.12$	$0.02 \pm 0.05$	$0.02 \pm 0.04$	RSF

Columns: (1) Galaxy identifier. (2)–(7): Gradients of the UV colour-index relations. (8): UV–optical radial colour profiles classification. RSF: recent star formation. UVX: UV upturn.

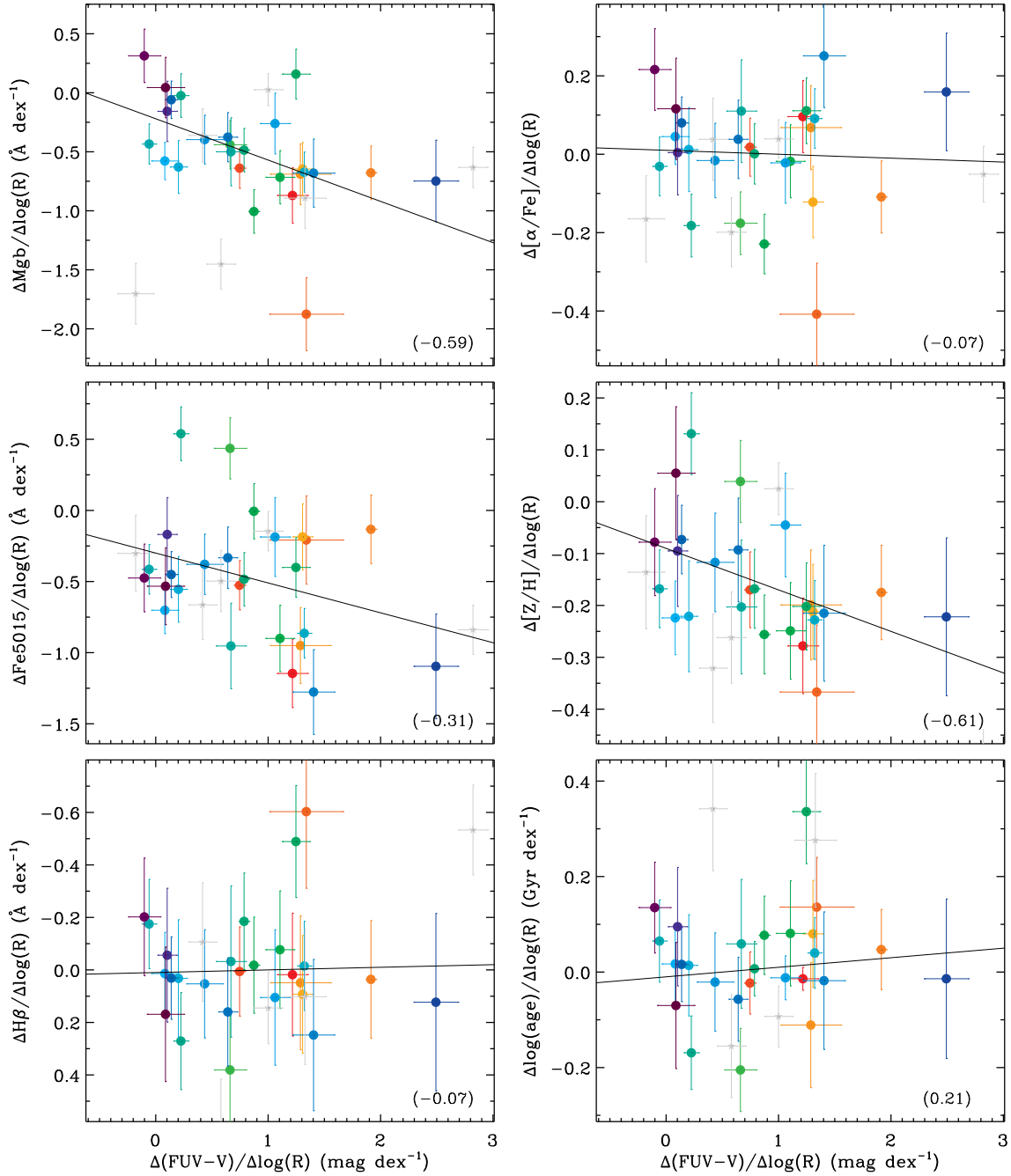


**Figure 6.** Same as Figure 1 but for the FUV–V logarithmic internal radial colour gradient versus the *measured* and *derived* stellar population gradients of the sample galaxies. The gradients of Mgb (*top-left*), Fe5015 (*middle-left*), H $\beta$  (*bottom-left*),  $[\alpha/\text{Fe}]$  (*top-right*),  $[\text{Z}/\text{H}]$  (*middle-right*) and age (*bottom-right*) are shown as a function of the FUV–V colour gradient. Quiescent galaxies ( $\text{H}\beta_{\text{Re}/2} \leq 1.8 \text{ \AA}$ ) are shown as solid circles, while galaxies with a young population are shown as grey stars. The solid line in each panel is a fit to the quiescent galaxies, and the correlation coefficient is reported in the bottom-right corner.

the effective radius (see Figure 1 of Paper XIII) and listed in Table 4. This is unlike the classification of Paper XIII, that considered much larger radial ranges, because SAURON covers each galaxy only up to about one effective radius. The classification differences between Paper XIII and this paper thus arise from different radial ranges considered. To select purely old galaxies, we first exclude galaxies with recent star formation as listed in Table 1 of Paper XIII.

Galaxies included in this category are NGC 474, 1023, 2974, 3032, 4150, 4459, 4526, 4550 and 7457. We then consider the NUV–V radial colour profiles. As discussed in Section 3.3 of Paper XIII, NUV–V colours usually show negative slopes due to the gradients of the underlying stellar populations, mainly in age and metallicity. This age-metallicity degeneracy is well-known and it is difficult to distinguish the effects of a small change in age from those of

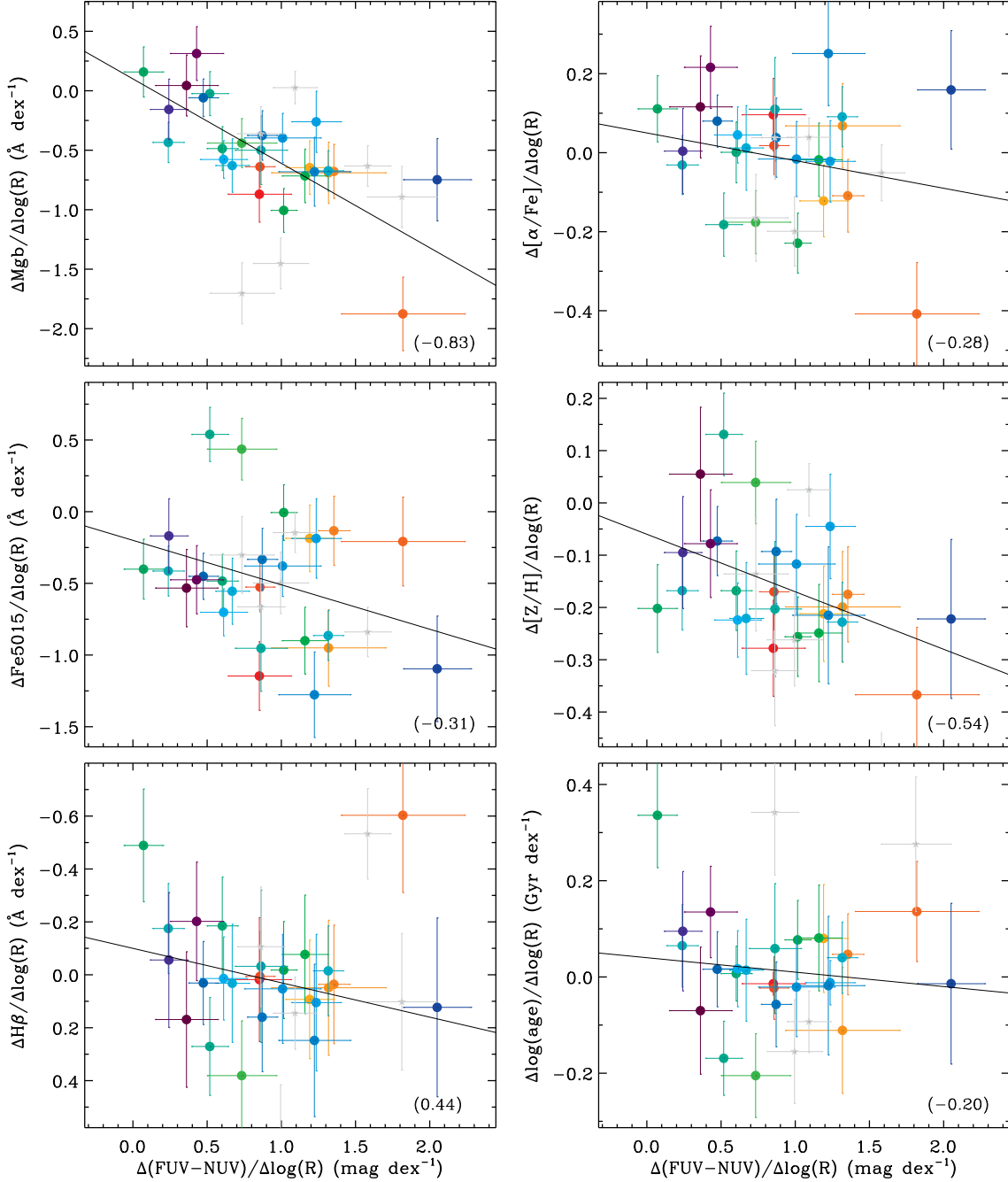


**Figure 7.** Same as Figure 6 but for the FUV–NUV colour.

a small change in metallicity. Therefore, we classify a galaxy as an age-metallicity degeneracy galaxy if its NUV–V profile is below  $5.0 \text{ mag arcsec}^{-2}$  around the effective radius only. These galaxies include NGC 5813, 5831 and 5845. Secondly, we consider the FUV–NUV and FUV–V profiles inside the effective radius. If a galaxy has a central region with  $\text{FUV-NUV} < 0.9 \text{ mag arcsec}^{-2}$  and  $\text{FUV-V} < 6.21 \text{ mag arcsec}^{-2}$  then, following the new classification scheme of Yi et al. (2011), we classify it as a UV upturn galaxy. These galaxies are NGC 2695, 4278, 4374, 4486, 4552, 4564, 4621, 5198, 5846 and 5982. Finally, we classify the remaining galaxies as UV-weak galaxies. Galaxies in-

cluded in this category are NGC 524, 821, 2699, 2768, 4387, 4458, 4473, 4477, 4546, 4570, 5308 and 5838.

Furthermore, we calculate the gradients of the UV colour-index relations (e.g.  $\Delta(\text{Mg } b)/\Delta(\text{FUV-V})$ ) for each individual galaxy using least-square fits (see Table 4) in the same way as described in Section 3.3. We note that the values of e.g.  $[\Delta(\text{Mg } b)/\Delta(\log(R))]$  are not equal to those of  $[\Delta(\text{Mg } b)/\Delta(\log(R))]/[\Delta(\text{FUV-V})/\Delta(\log(R))]$  listed in Table 2.

In Figure 9, we show the histograms of the Mg *b* and [Z/H] gradients with respect to the UV colours of individual galaxies (e.g.  $\Delta(\text{Mg } b)/\Delta(\text{FUV-V})$ ). We present the

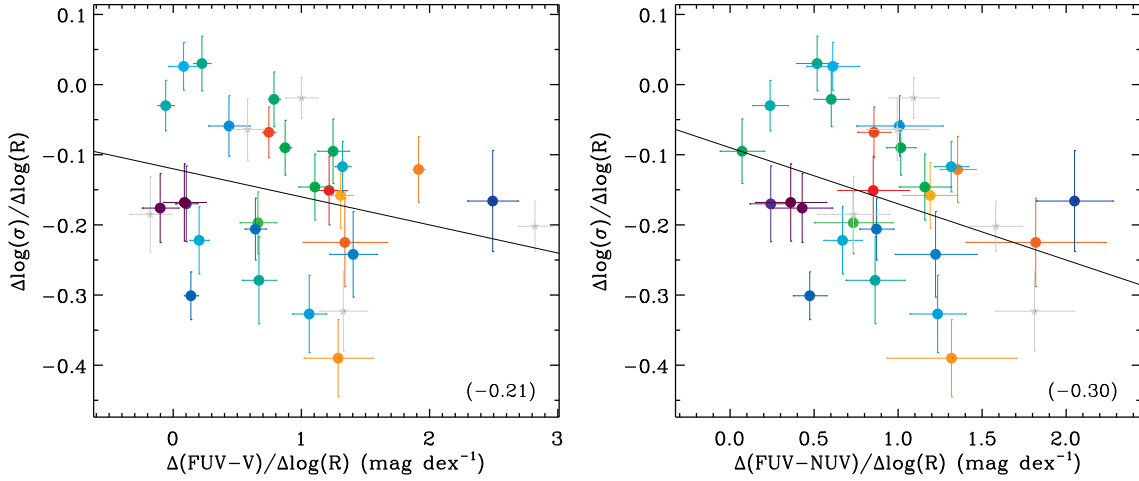


Figure 8. Same as Figures 6 and 7 but for the stellar velocity dispersion.

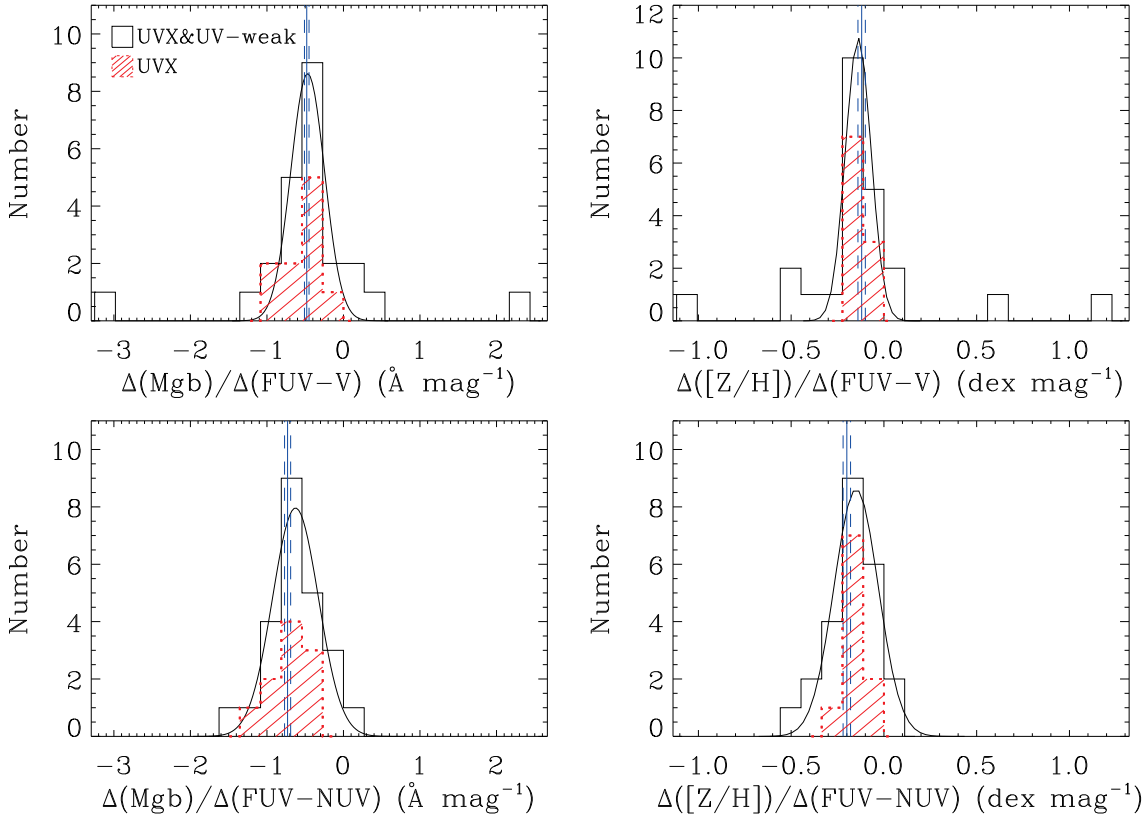


Figure 9. Histograms of the individual gradients of the UV colour-line index relations for the sample galaxies. The black solid lines are Gaussian fits to all quiescent galaxies. The blue vertical solid lines show the global gradients determined from fitting the luminosity-weighted galaxy profiles (solid lines in Figures 1 and 3), while the dashed lines indicate the associated uncertainties.

cases of  $Mgb$  and  $[Z/H]$  only, showing the tightest correlations in Figures 6 and 7. These diagrams are useful to test whether the individual galaxy gradients (local gradients) follow the global correlations (solid lines in Figures 1 and 3). The black histograms represent UV-weak and UV upturn galaxies, whereas the red shaded histograms show UV upturn galaxies only. We also fit Gaussians to the UV-weak and UV upturn galaxy gradient distributions and plot

them as black solid lines in each panel. The blue vertical solid lines show the global gradients (solid lines in Figures 1 and 3), while the blue dashed lines indicate the associated uncertainties.

If the global correlations (i.e. between galaxies) also apply locally within galaxies, the means of the Gaussian fits should be consistent with the global gradients. As discussed in Section 3.1, our global correlations are consistent with



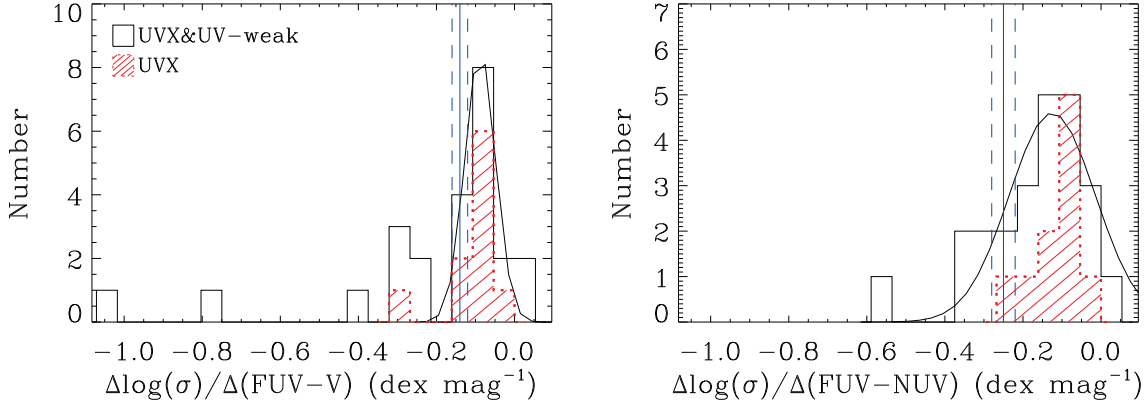


**Figure 10.** Same as Figure 9 but for the UV colour–stellar velocity dispersion relations. The blue vertical solid lines show the global gradients determined from fitting the luminosity-weighted galaxy profiles (solid lines in Figure 4).

those of Paper XVIII (determined from a fit to  $R_e/2$  aperture values for quiescent galaxies). For example, the slopes of the best-fit  $(FUV-NUV)-Mgb$ ,  $(FUV-NUV)-Fe5015$  and  $(FUV-NUV)-H\beta$  relations based on integrated properties are  $-0.64 \pm 0.12$ ,  $-0.21 \pm 0.17$  and  $0.20 \pm 0.08 \text{ \AA mag}^{-1}$ , whereas our global slopes are  $-0.73 \pm 0.04$ ,  $-0.36 \pm 0.06$  and  $-0.19 \pm 0.02 \text{ \AA mag}^{-1}$ , respectively. We note that the distributions of the individual galaxy gradients are consistent with the global gradients within the errors, although the distributions are considerably broader (Figure 9). For example, the global gradient for  $(FUV-V)-Mgb$  is  $-0.48 \pm 0.03 \text{ \AA mag}^{-1}$ , whereas the mean of the Gaussian fit to the local gradient distribution is  $-0.46 \text{ \AA mag}^{-1}$ , with an rms of  $0.21 \text{ \AA mag}^{-1}$ . Comparing the black and red shaded histograms, one can see that the distributions of the UV upturn galaxies are narrower than those of the UV-weak galaxies.

Similarly to Figure 9, Figure 10 shows the histograms of the stellar velocity dispersion gradients with respect to the UV colours of UV-weak and UV upturn galaxies. In the case of the velocity dispersion, however, the global gradients (vertical solid lines) are different from the local gradients (i.e. individual galaxies). This implies that the UV strength is not highly dependent on structural or dynamical properties.

### 3.4 Multi-dimensional relations

Figures 1–3, 6 and 7 show that the  $(FUV-NUV)-Mgb$  relation is the tightest correlation. We now consider multiple-parameter relations analogous to the fundamental plane (Djorgovski & Davis 1987; Dressler et al. 1987). Three-parameter relations are not trivially expected in the absence of *a priori* physical foundations, such as the virial theorem in the case of the Fundamental Plane. To minimise biases arising from the very different definitions and hence dynamic ranges of the parameters considered (e.g. line strengths, stellar population properties, velocity dispersion and colours), we normalize each quantity to yield an observed range of 1.0. For example, the observed range of  $FUV-V$  is roughly 4.7 to 7.3 mag (a difference of 2.6 magnitudes), and so in the abscissa of Figure 11, 0.0 means 2.6 mag bluer (UV stronger) than 1.0. Likewise, for the ordinate of the bottom-left plot, the observed range of  $Mgb$  is roughly 3.2 to 5.3  $\text{\AA}$  (a differ-

ence of 2.1  $\text{\AA}$ ), and that of  $\log(\sigma/\text{km s}^{-1})$  is roughly 1.9 to 2.5 (a difference of 0.6).

We have explored a number of parameter combinations and present some cases showing tight correlations in Figures 11 and 12.

The correlation coefficients reported in the bottom-right corner of each panel in Figures 11 and 12 are not much better (i.e. larger) than the simple one-parameter fits shown in Figures 1 and 3. This means that the relative FUV strength is not significantly better described when a third parameter is employed. This is in agreement with our finding in Paper XVIII, that it is stellar population properties rather than galaxy dynamical properties that govern the UV strength.

## 4 THE UV-INDEX RELATIONS

In summary, the results presented in Section 3 indicate tight local and global correlations between UV colours and  $Mgb$  and marginal correlations between UV colours and  $[Z/H]$ . These UV- $Mgb$  and UV- $[Z/H]$  relations are all the more significant because the global gradients are consistent with the local gradients. If the UV strength is related to the Mg line strength, galaxies with larger Mg gradients should have larger UV colour gradients, and the global gradient across galaxies should be consistent with the local gradients of individual galaxies as observed. Therefore, our results suggest that Mg is a main driver of the UV upturn or Mg and the UV upturn share the same primary driver, and the correlations between UV colours and  $[Z/H]$  can be understood by the role of Mg in the  $[Z/H]$  measurement.

Mg being the most representative  $\alpha$  element, it is puzzling that  $[\alpha/Fe]$  does not show a clear correlation with UV. Meanwhile, it should be noted that Carter et al. (2011) found good correlations between integrated  $FUV-NUV$  colours and integrated  $[\alpha/Fe]$  and  $[Z/H]$ . The weak correlations between the FUV colours and  $[\alpha/Fe]$  in this paper may be due to the fact that the  $\alpha$ -element is not directly measured from line strengths but derived from model fitting and so much more difficult than measuring a single metal line (e.g.  $Mgb$ ). Furthermore, the stellar population properties ( $[\alpha/Fe]$ ,  $[Z/H]$  and age) depend on the stellar models

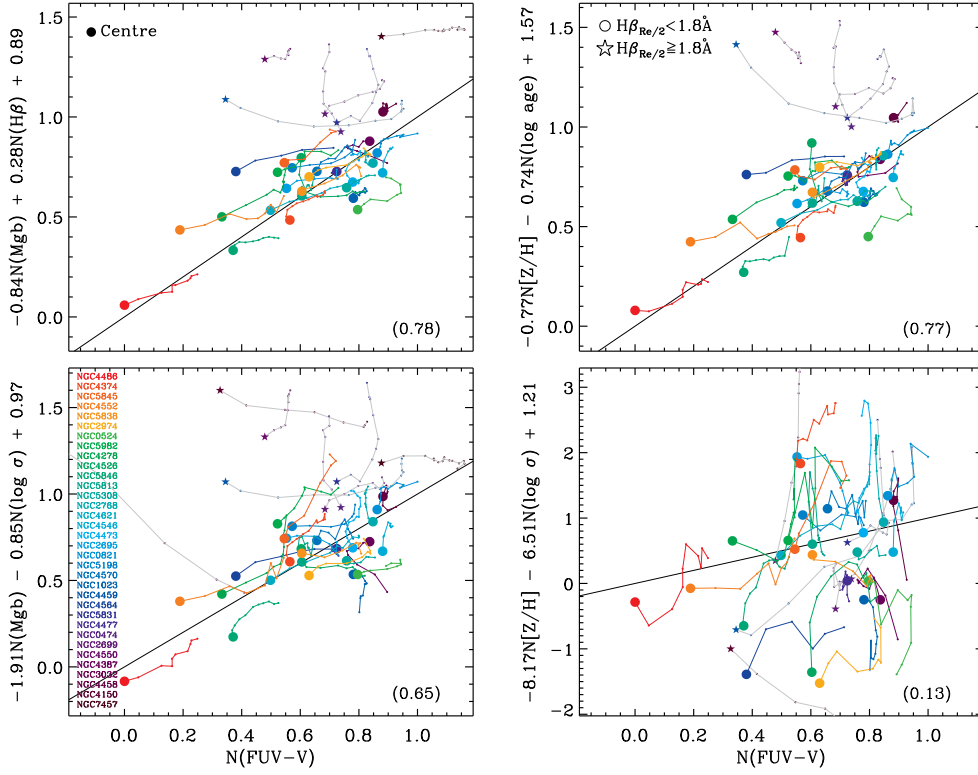


**Figure 11.** Edge-on views of the best-fit planes for selected three-parameter relations. The correlation coefficient is given in the bottom-right corner of each panel. The multi-parameter correlations shown are not much tighter than the simple one-parameter fits shown in Figures 1 and 3.

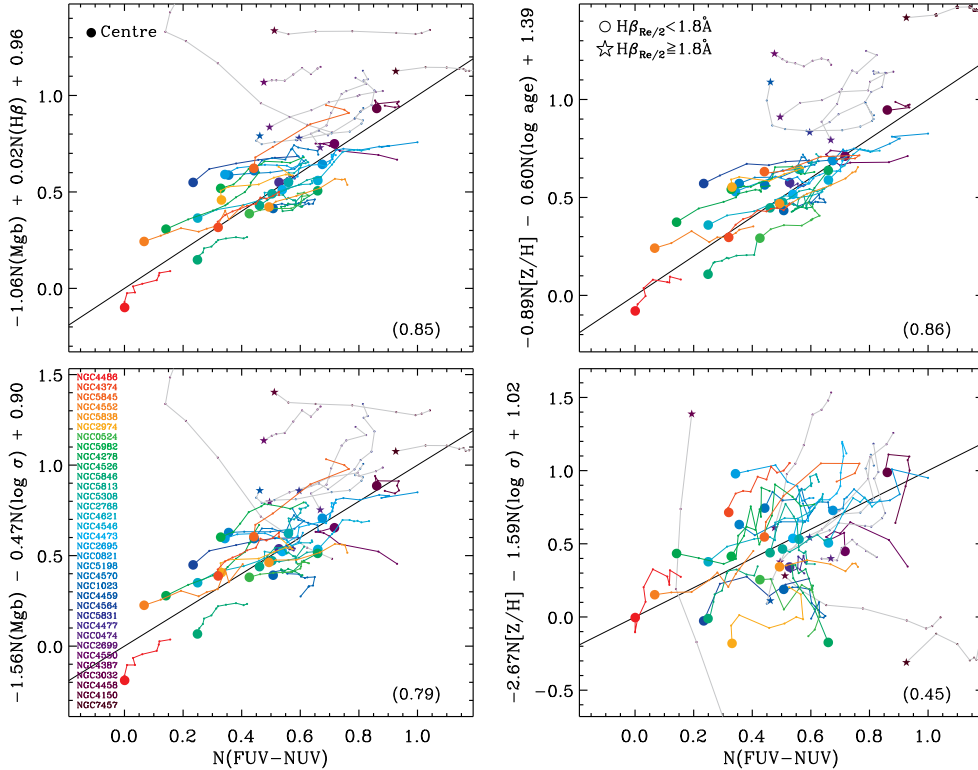


**Figure 12.** Same as Figure 11 but for the FUV-NUV colour.

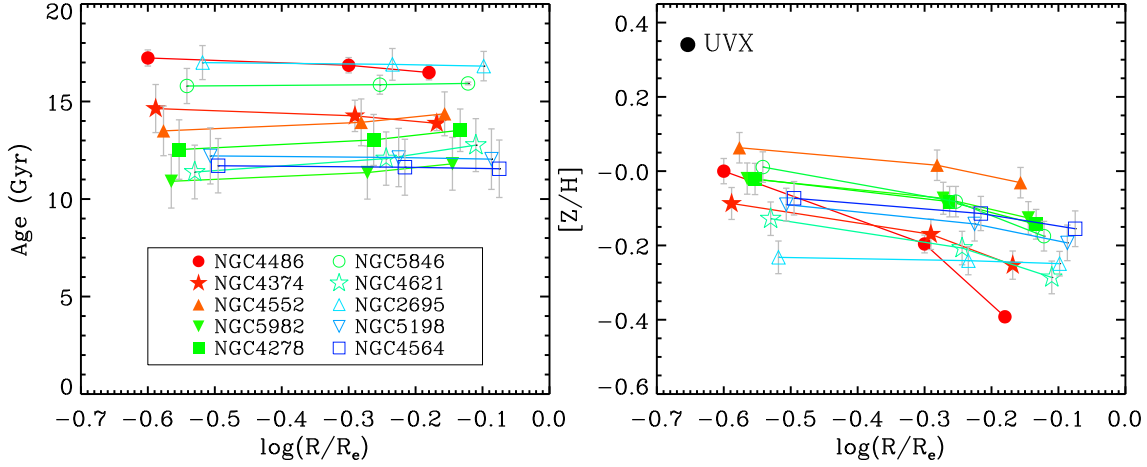


**Figure 13.** Radial profiles of age and metallicity ( $[Z/H]$ ) for UV upturn galaxies. The values are derived from NUV-defined elliptical annuli at  $R_e/4$ ,  $R_e/2$  and  $2R_e/3$ . Each profile is given a slightly different  $x$ -axis offset for clarity.

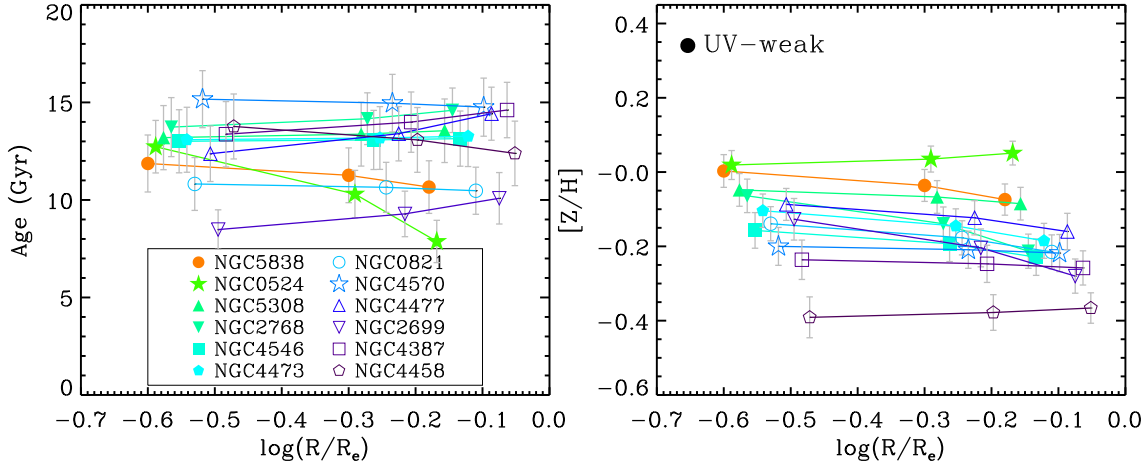


**Figure 14.** Same as Figure 13 but for UV-weak galaxies.

and spectral library adopted (see e.g. Coelho et al. 2007; Percival et al. 2009).

Given the reasonably-clear correlation between  $[Z/H]$  and UV colours, the apparently-weak correlation shown by Fe5015 and UV colours seems mysterious. A possibility is that Fe5015 may not be a robust tracer of  $[Z/H]$  because it is heavily contaminated by poorly understood absorption lines in this band (Lee et al. 2009).

We have also shown that global correlations exist between UV-related colours and the  $H\beta$  line strength, but we find no correlation between UV-related colour gradients and internal  $H\beta$  gradients. This can also be explained by metallicity effects on  $H\beta$  as discussed in Section 3.1.

Given the above, the metallicity gradients of UV upturn galaxies must be preserved to the present day. Is this possible in the hierarchical paradigm? Hopkins et al. (2009) carried out simulations and claimed that metallicity gradients are only weakly affected by both wet and dry mergers. Di Matteo et al. (2009) also argued that metallicity gradients can be preserved in major dry mergers if the metallicity gradient of companion is sufficiently steep.

Lastly, we point out that galaxies having recent star formation are outliers in the UV- $Mgb$  and UV- $[Z/H]$  relations; they usually have lower  $Mgb$  and  $[Z/H]$  values. It is therefore clear that tight UV- $Mgb$  and UV- $[Z/H]$  relations are only present for quiescent galaxies.

## 5 ORIGIN OF THE UV UPTURN

### 5.1 Stellar population parameters from line strengths

If different UV strengths are caused by different stellar population properties, this implies a difference between the stellar populations of UV upturn and UV-weak galaxies. To attempt to understand the conditions that create the observed UV upturns, we explore the stellar population parameters after separating quiescent galaxies into UV upturn and UV-weak galaxies, based on their UV radial colour profiles as discussed in Section 3.3.

Figure 13 shows the age and  $[Z/H]$  values of UV upturn galaxies at three different radii. To derive these stellar

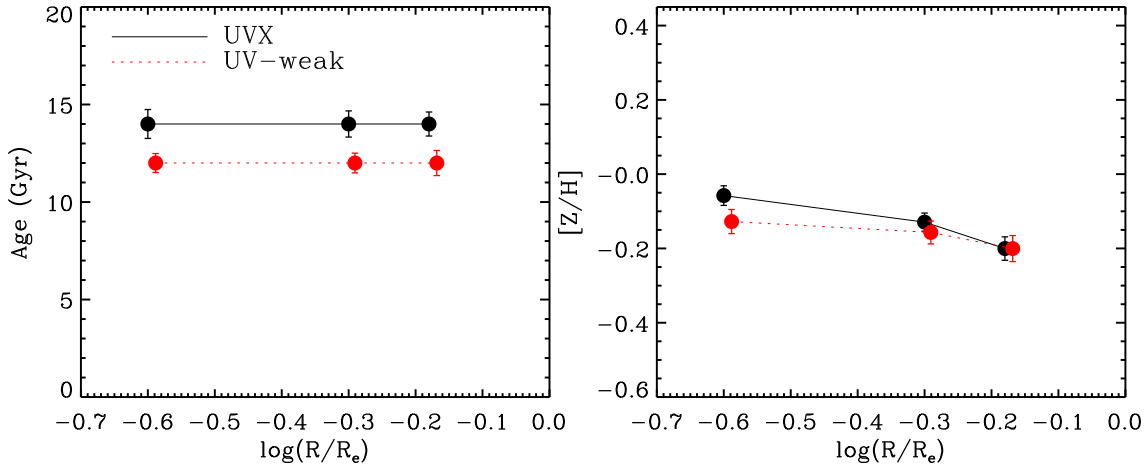


**Figure 15.** The mean radial age and metallicity profiles of UV upturn (black solid lines) and UV-weak (red dotted lines) galaxies based on the derived stellar population parameters from Paper XVII.

population parameters, we used here NUV-defined elliptical annuli of semi-major axes  $R_e/4$  (i.e. central),  $R_e/2$  (i.e. intermediate) and  $2R_e/3$  (i.e. outskirts), respectively. For clarity, each profile is given a slightly different  $x$ -axis offset. In UV upturn galaxies, the *derived* ages extend from roughly 11 to 17 Gyr. In the case of  $[Z/H]$ , the range is roughly  $-0.25$  to  $+0.05$ . We note that the age gradients are generally flat, whereas significant metallicity gradients exist.

Similarly to Figure 13, Figure 14 shows the age and  $[Z/H]$  gradients of UV-weak galaxies. The age gradients are again nearly flat, even though the metallicity gradients are weaker than those of UV upturn galaxies.

For comparison, we construct the mean radial age and metallicity profiles for the samples of UV upturn and UV-weak galaxies. The results are shown in Figure 15; the errors correspond to the standard deviations about the mean. There is a notable difference in age between the two samples (left panel), and a slight  $[Z/H]$  difference (right panel), especially in the central regions. Based on this, one might think that it is the age difference that governs the UV strength. However, without a radial age gradient, age alone cannot explain the central concentration of FUV light observed. Metallicity gradients are steep, especially in UV upturn galaxies, and so are probably essential to explain the centrally-concentrated FUV excess (as suggested in Sections 3 and 4).

## 5.2 New stellar population parameters from colours

If it is indeed stellar population properties that govern the UV strength of a quiescent galaxy, as we concluded in Sections 3 and 4, then the same stellar population models should be able to reproduce the UV relations for both integrated and internal properties. To find the range of age and metallicity that reproduce the observed UV properties, we attempt to fit the observed colour profiles (rather than line strengths) with the stellar population synthesis models of Yi (2003) and Yi, Demarque & Oemler (1997, 1998) that were calibrated to reproduce the observed properties of the UV upturn phenomenon. These models are sensi-

tive to metallicity, age, stellar mass loss, helium enrichment ( $\Delta Y/\Delta Z$ ) and the distribution of stars on the HB (see e.g. Dorman, O’Connell & Rood 1995; Percival & Salaris 2011; Chung, Yoon & Lee 2011).

The comparisons between the observed colours and models are shown in Figures 16 and 17. The existence of strong radial gradients of UV colours within galaxies is well known (e.g. O’Connell et al. 1992; Ohl et al. 1998), and in early-type galaxies they are likely the result of underlying stellar population gradients, mainly in age or metallicity or both. Therefore, we consider two simple cases: (1) an age gradient and (2) a metallicity gradient.

In the case of the metal-rich model, suggesting that the metal-rich HB stars are the most likely UV sources (see Section 1; Greggio & Renzini 1990; Horch et al. 1992; Bressan et al. 1994; Dorman et al. 1995; Yi, Demarque & Kim 1997), we could not reproduce the observed colour gradients at all using an age gradient alone. However, if we consider an internal metallicity gradient (with no age gradient), metal-rich models are able to reproduce the observed colour profiles. We assume, therefore, that the internal colour gradients of quiescent early-type galaxies are the result of simple metallicity gradients. The overall age of an individual galaxy is permitted to vary over the range 1 to 20 Gyr.

To constrain the age and metallicity of each galaxy, we thus fit the model to the observed FUV, NUV and  $V$  surface brightnesses at the same three radii used previously (center ( $R_e/4$ ), intermediate radius ( $R_e/2$ ) and outskirts ( $2R_e/3$ )), and compute the associated  $\chi^2$  statistics to obtain a probability distribution of the age and metallicity. Figure 16 shows the observed FUV–NUV and FUV– $V$  colour profiles (filled symbols) and the best-fit model profiles (solid lines) of NGC 4552 (blue triangle), 4278 (black circle) and 4477 (red diamond). Three open symbols of each galaxy represent the three fitted regions. This figure shows that we have found a plausible range of metal-rich model parameters that is capable of reproducing the observed amplitude of the UV upturn with the conventional values of  $\Delta Y/\Delta Z = 2.5$ ,  $\eta = 0.7$  and  $[\alpha/\text{Fe}] = 0.0$ .

Metal-poor models, suggesting that the dominant UV

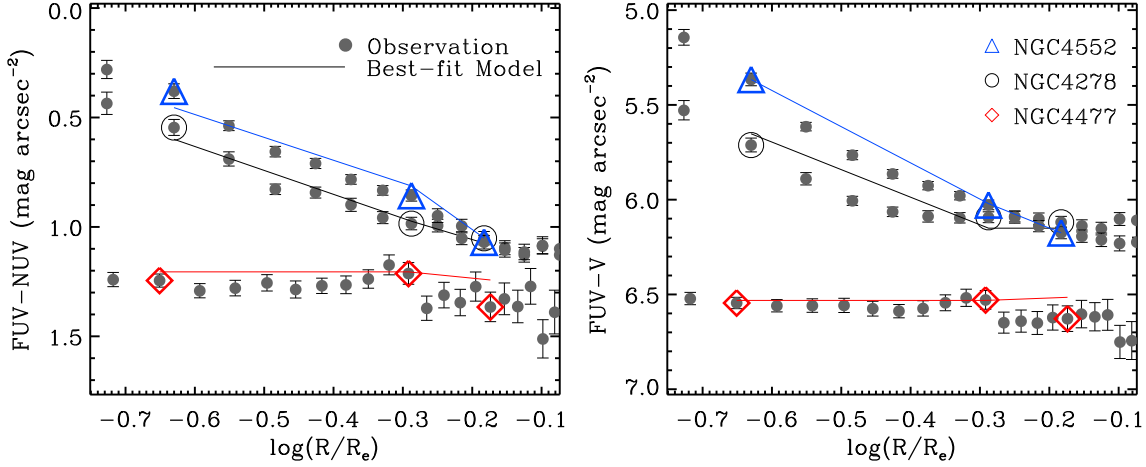


**Figure 16.** Comparison between the observed colours and metal-rich models of three sample galaxies (NGC 4552, 4278 and 4477). The FUV–NUV (left) and FUV–V (right) colours of each galaxy are shown as a function of radius. To derive the age and metallicity at a given radius, we fit the observed colours with the stellar population synthesis models of Yi (2003). Three different regions for each galaxy are used (open symbols; center, intermediate radius and outskirts). The best-fit model is shown as a solid line.

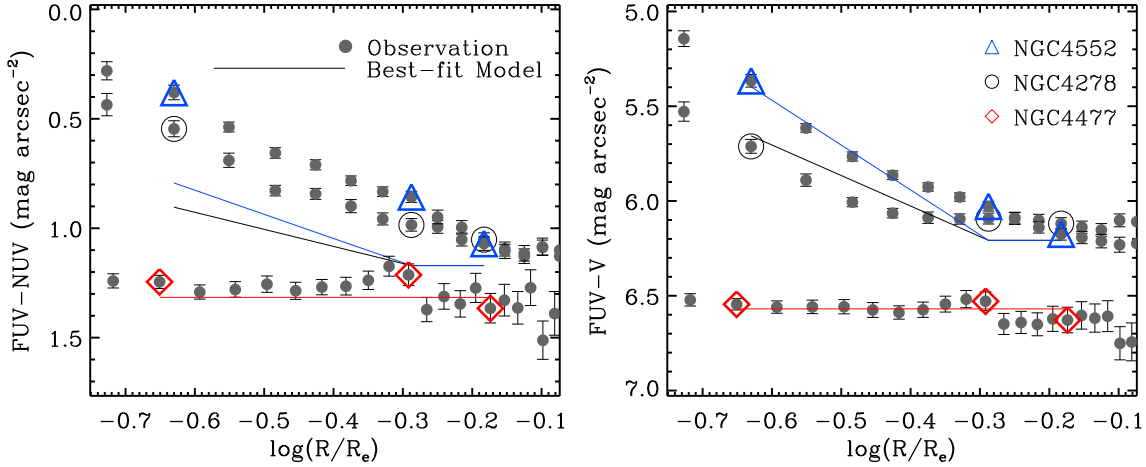


**Figure 17.** Same as Figure 16 but for the metal-poor model.

sources are older and metal-poor HB stars and their post-HB progeny (see Section 1; Lee et al. 1994; Park & Lee 1997; Buzzoni & González-Lópezlira 2008), fail to reproduce the observed surface brightnesses of UV upturn galaxies (e.g. NGC 4552 and 4278) when we consider age and metallicity gradients, as shown in Figure 17, although this depends on the adopted models (see e.g. Park & Lee 1997). We note that the model-fit for UV weak galaxy (e.g. NGC 4477) based on metal-poor models is also reasonably good. A number of recent studies found peculiar globular clusters having EHB stars that can be explained by the presence of super-helium-rich populations (Lee et al. 2005, 2007), which could also be a copious source of FUV flux. Indeed, Chung et al. (2011) claimed that their models with helium-enhanced subpopulations can reproduce the observed spectra of NGC 4552 and 4649. To perform the same test for this metal-poor but helium enhanced hypothesis, however, require super-helium-rich stellar population models which are not fully available yet.

Analogously to Figure 13, the best-fit values of age and metallicity based on metal-rich models, for all galaxies classified as UV upturn from their radial colour profiles, are shown in Figure 18. For clarity, the profiles are again given slight offsets with respect to each other along the  $x$ -axis. Errors show parameter values within  $1\sigma$  of the best-fit model. According to these models, the age range is 9 to 12 Gyr and the metallicity range is roughly  $-0.05$  to  $+0.28$ . Similarly to Figures 14 and 18, Figure 19 shows best-fit values of age and metallicity for UV-weak galaxies. In this case, the range of ages is 9 to 11 Gyr, with metallicities of roughly  $-0.27$  to  $+0.20$ .

Like Figure 15, Figure 20 shows the mean stellar population properties and the standard deviations about the means for UV upturn and UV-weak galaxies (filled squares). According to the models, the mean stellar age of UV-upturn galaxies (black solid lines) is about 11 Gyr and their central regions have a metallicity distribution peaking around 0.2, while at the effective radius the metallicities decrease to



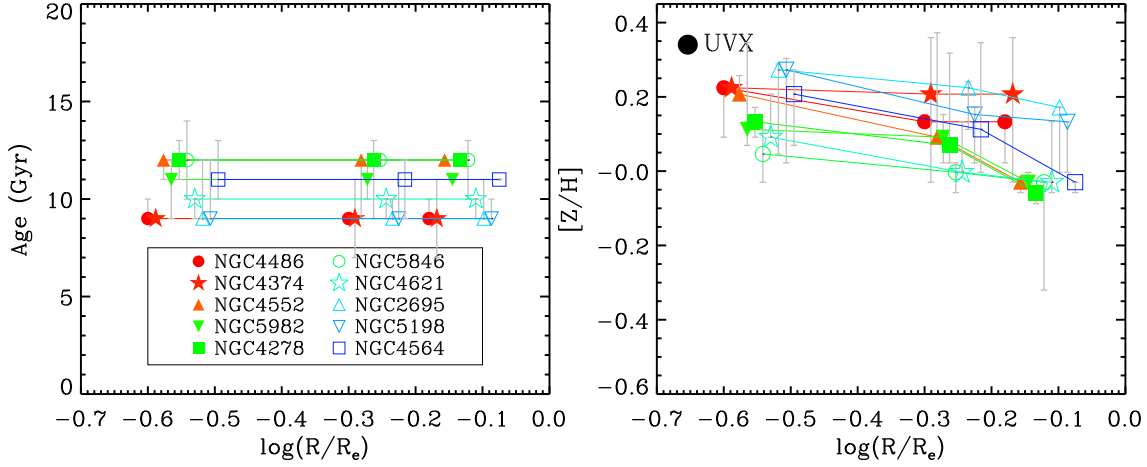


**Figure 18.** Radial profiles of age and metallicity for UV upturn galaxies, as derived from fits to the observed colours and the stellar population synthesis models of Yi (2003) at  $R_e/4$ ,  $R_e/2$  and  $2R_e/3$ . Each profile is given a slightly different  $x$ -axis offset for clarity.

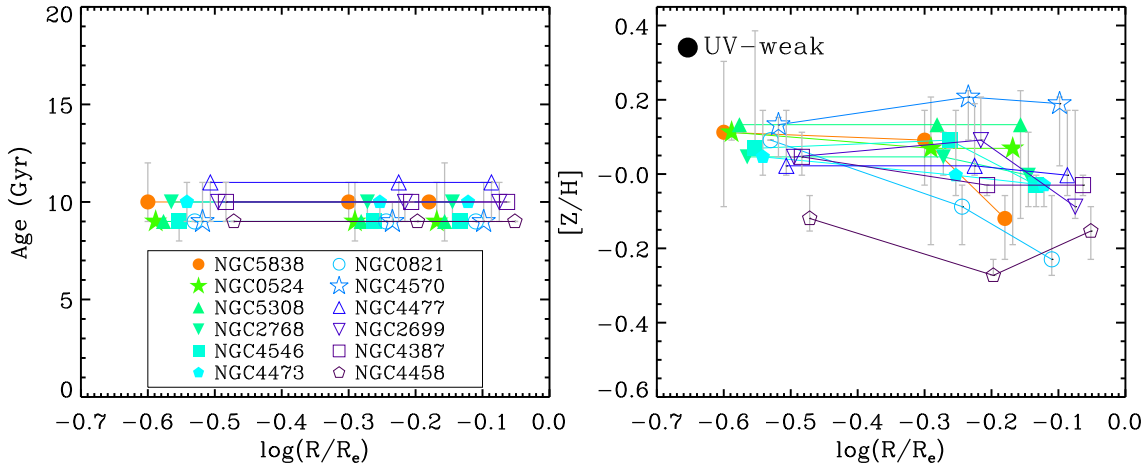


**Figure 19.** Same as Figure 18 but for UV-weak galaxies.

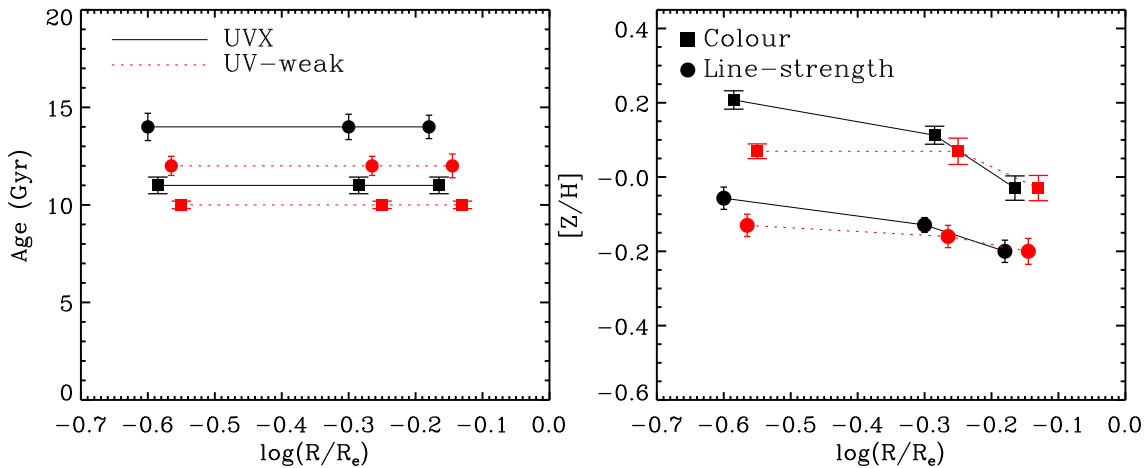


**Figure 20.** The mean radial age and metallicity profiles of UV upturn (black solid lines) and UV-weak (red dotted lines) galaxies based on colour fits and the models of Yi (2003) (filled squares). For comparison, we also show the mean ages and metallicities of UV upturn and UV-weak galaxies based on the derived stellar population parameters of Paper XVII (filled circles; see Figure 15).

slightly sub-solar. UV-weak galaxies (red dotted lines) have a similar mean stellar age but significantly smaller metallicity gradients compared to UV upturn galaxies. The metallicity difference between UV upturn and UV-weak galaxies in the central regions produces the difference in the UV upturn strength. The UV upturn phenomenon seems indeed to be due to stellar population properties.

For comparison, we plot again the mean ages and metallicities derived from spectral line strengths (see Figure 15) as filled circles. In both cases, UV upturn galaxies are slightly older than UV-weak galaxies and the metallicities of UV upturn and UV-weak galaxies reveal differences, especially in the central regions. The trends of age and metallicity derived from spectral line strengths and colours are thus similar, but the actual values reveal significant differences. This can be explained in terms of the age-metallicity degeneracy.

The previous SAURON work of Paper XVII found that models with very high ages ( $\approx 14$  Gyr) match the high Mg absorption of UV upturn galaxies. In contrast, through our colour fitting method, we find that slightly younger ( $\approx 11$  Gyr) but more metal-rich models better reproduce the pronounced UV flux in the interiors of UV upturn galaxies. It is well known that line strengths and colour indices suffer from the age-metallicity degeneracy (Worthey 1994). Furthermore, as described in Section 2.3, we should not believe the absolute ages and metallicities returned by the models, even though they still allow us to make relative comparisons between galaxies. The model parameters derived from line strengths in Paper XVII (Section 5.1) and from colours here (Section 5.2) can thus probably be reconciled through the age-metallicity degeneracy.

Therefore, despite having failed to find the same parameter ranges when using spectral line strengths and colours, we do feel that we have found plausible parameters that reproduce the observed radial colour profiles of UV upturn and UV-weak galaxies. Furthermore, it is important to reproduce the UV relations for internal properties using the stellar population synthesis models of Yi (2003), which are specifically designed to explain the UV upturn phenomenon. Notably, our models reproduce the range of UV strengths among elliptical galaxies by varying the metallicity. In the context of the Yi (2003) models, the UV upturn is a stellar phenomenon associated with the metal-rich (high Mg *b* line strength) population of early-type galaxies, and the UV-bright central regions of giant elliptical galaxies (e.g. NGC 4552 and 4278) are enhanced in metals by roughly 60% compared to the UV-weak parts.

## 6 SUMMARY

We have used ultraviolet photometry from *GALEX*, ground-based optical photometry from MDM and ground-based optical integral-field spectroscopy from SAURON to study the UV-line strength and UV-stellar population relations of 34 early-type galaxies from the SAURON sample. Our main advantage in exploring these correlations is that all photometric and spectroscopic measurement are derived using the same ellipses and apertures.

First, we have found that passively-evolving galaxies show clear correlations between the colours involving FUV (FUV-*V* and FUV-NUV) and the Mg *b* and H $\beta$  absorption

line strength indices, as well as the metallicity [Z/H], and that these correlations are strongest for FUV-NUV. This result is supported by a pixel-by-pixel analysis. This suggests that either Mg is a main driver of the UV upturn or Mg and the UV upturn share the same primary driver, and that the correlation between the UV colour and metallicity is explained by the role of Mg in the metallicity measurement. Likewise, the correlation of the UV colour with H $\beta$  can be explained by the metallicity effect on H $\beta$ .

In addition, we have also derived logarithmic internal colour, *measured* line strength and stellar population gradients for each galaxy and again found a strong dependence of the FUV-*V* and FUV-NUV colours on the Mg *b* line strength, as well as on metallicity. Moreover, the Mg *b* and [Z/H] global gradients with respect to the UV colours (e.g.  $\Delta(\text{Mg } b) / \Delta(\text{FUV}-V)$ ) are consistent with their respective local gradients, implying that the global correlations also hold locally within galaxies.

Finally, if the UV strength is indeed governed by stellar population properties, then the same models should be able to reproduce the UV relations for both integrated properties and internal properties (within each galaxy). From simple models based on UV-optical colour fits of UV upturn and UV-weak galaxies, we have identified a plausible range of parameters that reproduces the observed radial colour profiles of each galaxy type. In these models, the UV upturn is a stellar phenomenon associated with the metal-rich (high Mg *b* line strength) population of early-type galaxies, and the inner parts (UV-bright regions) of giant elliptical galaxies are enhanced in metals by roughly 60% (e.g. NGC 4552 and 4278) compared to the outer parts (UV-weak regions). We stress here that stars originating the UV upturn phenomenon are detected in the central region of galaxies (especially within  $R_e/4$ ), and therefore they are contributing  $< 20\%$  of the total stellar light. This means that the UV upturn phenomenon is naturally produced if the galaxy has a small fraction of Mg enhanced populations. Assuming that the galaxy has a 10% metal-enhanced population, it cannot make a significant change in the overall metallicity of the galaxy, but this population can evolve to the FUV excess stars.

Without doubt, we now have much more information on the UV upturn than a decade ago. However, there still are many puzzles. For example, it is surprising that the  $\alpha$ -enhancement ( $[\alpha/\text{Fe}]$ ) does not show a correlation with UV strength, considering that Mg *b* shows a tight correlation with UV colours and [Z/H] also shows a marginal correlation. Improvements over the work presented in this paper will come from a more careful population modelling analysis.

Our achievements here were mainly obtained through the spatially-resolved analyses that have just recently become possible. A critical weakness of our work however is the poor spatial resolution of the UV data. Breakthroughs will be guaranteed when higher spatial resolution (arcsec scale) FUV data become available, hopefully in the near future.

## ACKNOWLEDGMENTS

This work was supported by the National Research Foundation of Korea through the Doyak grant (No. 20090078756),

the SRC grant to the Center for Galaxy Evolution Research and the KASI grant given to SKY. MB acknowledges support from NASA through GALEX Guest Investigator program GALEX GI 04-0000-0109. MB and SKY are grateful to the Royal Society for an International Joint Project award (2007/R2) supporting this work. The STFC Visitors grant to Oxford also supported joint visits. JF-B acknowledges the support from the Ramón y Cajal Program as well as grant AYA2010-21322-C03-02 by the Spanish Ministry of Science and Innovation. GALEX is operated for NASA by the California Institute of Technology under NASA contract NAS5-98034. Photometric data were also obtained using the 1.3m McGraw-Hill Telescope of the MDM Observatory. Part of this work is based on data obtained from the ESO/ST-ECF Science Archive Facility. This project made use of the HyperLeda database (<http://leda.univ-lyon1.fr>) and the NASA/IPAC Extragalactic Database (NED) which is operated by the Jet Propulsion Laboratory, California Institute of Technology, under contract with the National Aeronautics and Space Administration.

## REFERENCES

- Bender R., Burstein D., Faber S. M., 1993, *ApJ*, 411, 153  
 Bernardi M., et al., 2003, *AJ*, 125, 1882  
 Bertola F., Capaccioli M., Holm A. V., Oke J. B., 1980, *ApJL*, 237, L65  
 Bohlin R. C., Cornett R. H., Hill J. K., Hill R. S., O’Connell R. W., Stecher T. P., 1985, *ApJL*, 298, 37  
 Bressan A., Chiosi C., Fagotto F., 1994, *ApJS*, 94, 63  
 Brown T. M., Ferguson H. C., Davidsen A. F., Doorman B., 1997, *ApJ*, 482, 685  
 Brown T. M., Bowers C. W., Kimble R. A., Ferguson H. C., 2000, *ApJ*, 529, L89  
 Bruzual G., Charlot S., 2003, *MNRAS*, 344, 1000  
 Bureau M., et al., 2011, in press, [Paper XVIII]  
 Burstein D., Bertola F., Buson L. M., Faber S. M., Lauer T. R., 1988, *ApJ*, 328, 440 [BBBFL88]  
 Buzzoni A., González-Lópezlira R. A., 2008, *ApJ*, 686, 1007  
 Carter D., Pass S., Kennedy J. Karick A. M., Smith R. J., 2011, *MNRAS*, 414, 3410  
 Cardelli J. A., Clayton G. C., Mathis J. S., 1989, *ApJ*, 345, 245  
 Chung C., Yoon S.-J., Lee Y.-W., 2011, *ApJL*, 740, L45  
 Code A. D., 1969, *PASP*, 81, 475  
 Code A. D., Welch G. A., Page T., 1972, in A. D. Code, ed, *Scientific Results from the Orbiting Astronomical Observatory (OAO-2)*. NASA SP-310, p. 559  
 Code A. D., Welch G. A., 1979, *ApJ*, 228, 95  
 Coelho P., Bruzual G., Charlot S., Weiss A., Barbuy B., Ferguson J. W., 2007, *MNRAS*, 382, 498  
 Colless M., Burstein D., Davies R. L., McMahan R. K., Saglia R. P., Wegner G., 1999, *MNRAS*, 303, 813  
 Di Matteo P., Pipino A., Lehnert M. D., Combes F., Semelin B., 2009, *A&A* 499, 427  
 Djorgovski S., Davis M., 1987, *ApJ*, 313, 59  
 Donas J., et al., 2007, *ApJS*, 173, 597  
 Dorman B., O’Connell R. W., Rood R. T., 1995, *ApJ*, 442, 105  
 Dressler A., Lynden-Bell D., Burstein D., Davies R. L., Faber S. M., Terlevich R. J., Vegner G., 1987, *ApJ*, 313, 42  
 de Zeeuw P. T., et al., 2002, *MNRAS*, 329, 513 [Paper II]  
 Emsellem E., et al., 2004, *MNRAS*, 352, 721 [Paper III]  
 Emsellem E., et al., 2007, *MNRAS*, 379, 401 [Paper IX]  
 Faber S. M., 1972, *A&A*, 20, 361  
 Faber S. M., 1983, *Highlights of Astronomy*, 6, 165  
 Falcón-Barroso J., 2011, *MNRAS*, in press [Paper XIX]  
 Gil de Paz A., et al., 2007, *ApJS*, 173, 185  
 Greggio L., Renzini A., 1990, *ApJ*, 364, 35  
 Han Z., Podsiadlowski Ph., Lynas-Gray A. E., 2007, *MNRAS*, 380, 1098  
 Han Z., Podsiadlowski Ph., Maxted P. F. L., Marsh T. R., 2003, *MNRAS*, 341, 669  
 Hopkins P. F., Lauer T. R., Cox T. J., Hernquist L., Kormendy J., 2009, *ApJS*, 181, 486  
 Horch E., Demarque P., Pinsonneault M., 1992, *ApJ*, 388, L53  
 Jeong H., et al., 2009, *MNRAS*, 398, 2028 [Paper XIII]  
 Kaviraj S., et al., 2007, *ApJS*, 173, 619  
 Kuntschner H., et al., 2006, *MNRAS*, 369, 497 [Paper VI]  
 Kuntschner H., et al., 2010, *MNRAS*, in press [Paper XVII]  
 Lee H.-c., et al., 2009, *ApJ*, 694, 902  
 Lee Y.-W., Demarque P., Zinn R., 1994, *ApJ*, 423, 248  
 Lee Y.-W., et al., 2005, *ApJ*, 621, L57  
 Lee Y.-W., Gim H. B., Casetti-Dinescu D. I., 2007, *ApJ*, 661, L49  
 Martin D. C., et al., 2005, *ApJ*, 619, L1  
 Maxted P. F. L., Heber U., Marsh T. R., North R. C., 2001, *MNRAS*, 326, 1391  
 Morrissey P., et al., 2005, *ApJ*, 619, L7  
 Morrissey P., et al., 2007, *ApJS*, 173, 682  
 O’Connell R. W., et al., 1992, *ApJ*, 395, L4  
 O’Connell R. W., 1999, *ARA&A*, 37, 603  
 Ohl R. G., et al., 1998, *ApJ*, 505, L11  
 Park J.-H., Lee Y.-W., 1997, *ApJ*, 476, 28  
 Percival S. M., Salaris M., Cassisi S., Pietrinferni A., *ApJ*, 690, 427  
 Percival S. M., Salaris M., 2011, *MNRAS*, 412, 2445  
 Peterson, R. C., 1976, *ApJL*, 210, L123  
 Rich R. M., et al., 2005, *ApJL*, 619, L107  
 Schawinski K., et al., 2007, *ApJS*, 173, 512  
 Schiavon R. P., 2007, *ApJS*, 171, 146  
 Schlegel D. J., Finkbeiner D. P., Davis M., 1998, *ApJ*, 500, 525  
 Smith, R. J., Lucey, J. R., Hudson, M. J., Bridges, T. J., 2009, *MNRAS*, 398, 119  
 Sohn S. T., O’Connell R. W., Kundu A., Landsman W. B., Burstein D., Bohlin R. C., Frogel J. A., Rose J. A., 2006, *AJ*, 131, 866  
 Terlevich R., Davies R. L., Faber S. M., Burstein D., 1981, *MNRAS*, 196, 381  
 Tinsley B. M., 1972, *A&A*, 20, 383  
 Thomas D., Maraston C., Bender R., 2003, *MNRAS*, 339, 897  
 Thomas D., Maraston C., Bender R., Mendes de Oliveira, C., 2005, *ApJ*, 621, 673  
 Trager S. C., Faber, S. M., Worthey, G., González, J. J., 2000, *AJ*, 119, 1645  
 Welch, G. A., 1982, *ApJ*, 259, 77  
 Worthey G., 1994, *ApJS*, 95, 107  
 Wyder T. K., et al., 2005, *ApJL*, 619, L15

- Yi S., Demarque P., Kim Y.-C., 1997, ApJ, 482, 677  
Yi S., Demarque P., Oemler, A. Jr., 1997, ApJ, 486, 201  
Yi S., Demarque P., Oemler, A. Jr., 1998, ApJ, 492, 480  
Yi S., Lee Y.-W., Woo J.-H., Park J.-H., Demarque P.,  
Oemler Jr. A., 1999, ApJ, 513, 128  
Yi S. K., 2003, ApJ, 582, 202  
Yi S. K., et al., 2005, ApJL, 619, 111  
Yi S. K., Lee J., Sheen Y.-K., Jeong H., Suh H., Oh K.,  
2011, ApJS, 195, 22